Distributed Networked Microgrids Power Flow

Fei Feng, *Student Member, IEEE*, Peng Zhang, *Senior Member, IEEE*, Yifan Zhou, *Member, IEEE* and Lizhi Wang, *Student Member, IEEE*

***Abstract*—An integrative power flow approach is established for networked microgrids. Our new contributions include: 1) A distributed augmented power flow (APF) algorithm for networked microgrids is devised to incorporate hierarchical control effects in/among microgrids; 2) Based upon APF, an enhanced distributed continuation power flow (CPF$^+$) algorithm is established to explore operating regions of droop coefficients and power interchanges for static voltage stability assessment; and 3) A programmable distributed platform is designed to coordinate power interchanges and support plug-and-play while protecting local customers' privacy. RTDS experiments validate the high fidelity of APF, while its scalability and convergence performance are verified on medium and large networked microgrids. Extensive tests demonstrate the effectiveness of CPF$^+$ in quantifying secure operation regions of networked microgrids.**

***Index Terms*—Networked microgrids, power flow, hierarchical control, RTDS verification.**

I. Introduction

MICROGRID is a promising paradigm for integrating distributed energy resources (DERs) and ensuring electricity resiliency due to its flexible and automatic operation [1]–[4]. However, an individual microgrid, because of limited capacity, could hardly serve as a dependable resiliency resource for densely populated communities in urban areas such as New York City. Networked microgrids, a cluster of microgrids integrated with interactive support and coordinated energy management, offer a promise to relieve power deficiencies in individual microgrids, support more local customers, and even black start neighboring energy infrastructures upon occurrence of a blackout [5]–[8]. At the heart of networked microgrids is an energy management system [9] where power flow calculation is a keystone function indispensable for making decisions regarding the best use of DERs for meeting customers' needs.

Power flows in networked microgrids largely depend on the operating modes (e.g. grid-connected or islanded mode) and control modes of DERs (e.g. droop control and secondary control) [10], [11]. In the grid-connected mode, power flow analysis of microgrids follows the same approach as that of distribution networks because those microgrids' voltages and frequency are supported by the main grid. In the islanded mode, hierarchical controls have been widely adopted in microgrids for power sharing and voltage regulation purposes [12]. To be specific, primary controls of each individual microgrid stabilize the network and establishes a proportional sharing of loads among DERs; secondary controls eliminate frequency and voltage deviations caused by primary controls. Meanwhile, power interchanges between microgrids can be regulated through a control layer on top of secondary controls within individual microgrids [13]. However, droop/secondary-based islanded networked microgrids have to maintain their voltages and frequency independent of a main grid, which still has yet to be fully addressed because: 1) Slack buses no longer exist because no DERs can always maintain a constant frequency because of insufficient capacity. 2) The hierarchical control modes of DERs change frequently, driven by power coordination and voltage regulation needs under uncertain DER and load profiles. 3) Frequently changing system structure and stringent data privacy requirements exist in today's microgrids. The aforementioned bottlenecks therefore requires a fully distributed yet control-incorporated power flow analysis of networked microgrids.

For an individual microgrid, different control modes have been proposed to support stable operations [14]. Correspondingly, derivative-based power flow methods are developed to consider droop based power sharing in islanded microgrids [15], [16]. Reference [17] introduces a Newton-trust-region based algorithm that accounts for the microgrid frequency. Similar droop-based algorithms have been extended to DC and hybrid microgrids [18]–[22].

Recently, a microgrid power flow considering secondary control modes (e.g. reactive power sharing, voltage regulation, smart tuning) has been developed by the authors [23]. Meanwhile, non-derivative power flow approaches (e.g. direct back/forward sweep, implicit Z_{bus}) are developed for islanded microgrids by introducing an adaptive swing bus to update voltage and frequency [17], [24]. The modified backward/forward sweep algorithms, however, apply only to radial or weakly meshed microgrids and cannot analyze meshed microgrids commonly adopted in densely populated areas [24], [25]. The revisited implicit Z_{bus} Gauss (GRev), although capable of handling meshed microgrids, suffers from large number of iterations under specific conditions, which may affect its scalability [26]. Reachable power flow is another newly developed power flow analysis tool for enclosing uncertain power flow states via a single reachability calculation [27], [28]. It also exhibits satisfactory efficacy in verifying the steady-state performance of microgrids under droop and secondary control. Nevertheless, none of the aforementioned power flow methods for individual microgrids could be utilized directly for networked microgrids because they are unable to model interface power coordination and voltage regulation among microgrids. Although the compositional power flow [29] allows backward/forward sweep to adjust boundary bus voltages, it can only regulate one tie line of a networked microgrid system

This material is based upon work supported by the U.S. National Science Foundation under Grant Nos. CNS-2006828, ECCS-2018492, OIA-2040599, and OIA-2134840.

The authors are are with the Department of Electrical and Computer Engineering, Stony Brook University, Stony Brook, NY 11794-2350, USA (e-mail: P.Zhang@stonybrook.edu).

This article has been accepted for publication in a future issue of this journal, but has not been fully edited. Content may change prior to final publication. Citation information: DOI 10.1109/TPWRS.2022.3175933, IEEE Transactions on Power Systems

because of the dependence on a swing bus.

A salient feature of networked microgrids is the capability of scheduling power interchange among microgrids via a hierarchical control scheme. Voltage collapses, however, may occur under extreme power delivery conditions due to excessive real or reactive power demands and subsequent control actions. Therefore, verifying feasible droop coefficients and interface powers are critical for resilient operations of networked microgrids. Previously, continuation power flow has been adopted in the static voltage stability analysis of distribution systems [30]–[33]. Ref [34] verified the capability of both non-derivative (Backward/forward-sweep-based) and Newton-based CPFs in solving the static voltage stability of distribution systems with different R/X ratios. By performing the predictor–corrector steps [35]–[37], CPF can potentially be used to explore the static voltage stability region of system operating parameters, such as load levels, controller coefficients, etc. Although modified continuation method is developed to incorporate load margin factor into individual microgrid power flow modeling [38], interface power exchange margin among microgrids can not be explored, because of its inability to incorporate hierarchical power sharing and voltage regulation effects [39].

To overcome the limitations of traditional power flow algorithms, this paper devises an augmented Newton-type networked microgrids power flow (APF) solution that is able to not only incorporate various hierarchical control modes but also process arbitrary grid topology including radial and meshed structures. Further, an enhanced continuation power flow (CPF$^+$) algorithm is established aiming at ensuring networked microgrids' resilience against static voltage instabilities. Our contributions in this paper are threefold:

- *A distributed, augmented Newton-type power flow (APF) formulation is derived to incorporate hierarchical control in networked microgrids.*
  APF establishes a thorough power flow formulation of droop/secondary-controlled networked microgrids. Modified Jacobian matrices are derived in a distributed manner to allow for automatic modeling under various control schemes, such as power sharing, voltage regulation and interface power exchange. APF eliminates the reliance on an adaptive swing bus to update voltage and frequency, fully supporting voltage adjustments of multiple tie lines. RTDS experiments are designed to verify the fidelity of APF.
- *A distributed CPF$^+$ algorithm is devised to quantify the effects of droop coefficient and power interchange on the static voltage stability of networked microgrids.*
  CPF$^+$ is capable of distributively calculating the acceptable operating regions of droop factor and power interchange factor in consideration of voltage stability, which provides a powerful tool for controller synthesis of networked microgrids.
- *A programmable distributed platform is constructed for networked microgrids power flow analysis.*
  The platform provides a software-defined architecture to achieve interface power coordination for APF and control factor updating for CPF$^+$. The distributed manner of this platform fully supports plug-and-play among microgrids and protects local customers' privacy.

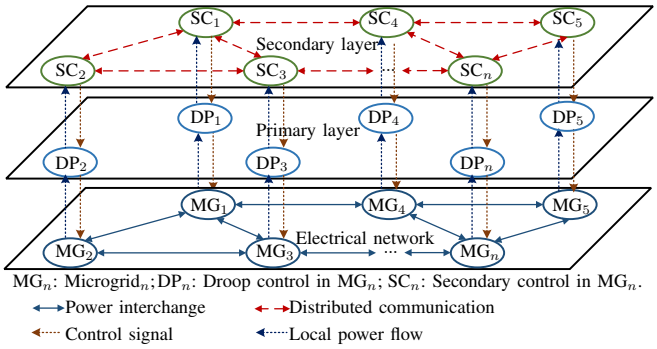

Fig. 1: Architecture of networked microgrids

The remainder of this paper is organized as follows: Section II devises the APF formulation, i.e., the networked microgrids power flow incorporating hierarchical control. Section III develops the CPF$^+$ algorithm and establishes the distributed power flow platform. Section IV focuses on case studies that verify the effectiveness and convergence performance of both methods, followed by the Conclusion in Section V.

II. Networked Microgrids Power Flow

A. Networked Microgrids Architecture

Generally, hierarchical control for networked microgrids consists of two layers to realize power management and voltage regulation (see Fig. 1).

1) Primary layer: When operating in islanded situations, DERs respond to the real and reactive power demand following the droop controls in the primary layer.

2) Secondary layer: The main functionality of secondary control is to mitigate the steady-state errors in droop control while it sometimes can also be used to achieve global power sharing among microgrids. When one microgrid suffers from power deficiency, neighboring microgrids could provide power support by communicating with each other [14].

The devised APF methodology considers power coordination of multiconnected microgrids by modeling different hierarchical control modes, as detailed in Subsection II.B and Subsection II.C.

B. Distributed APF Formulation

In APF, we introduce a new bus type named *DER buses* to formulate the DERs equipped with hierarchical control [23]. Different from the traditional PV and PQ buses, *DER buses* follow the hierarchical control logic to jointly achieve expected power sharing and voltage regulation.

1) Power Sharing Mode (PS): PS aims to realize a set of scheduled power interchanges between neighboring microgrids when a specific microgrid suffers power deficiency. The voltages at boundary buses connected with tie lines need to achieve certain target values.

To establish a fully distributed APF, leader DER buses are selected whose power outputs are regulated to eventually control the power interchanges through the tie lines[1]. The scheduled power interchange is realized by adjusting the boundary bus voltages of each microgrid. Without loss of generality, we assume that DER buses in microgrid i are to

This article has been accepted for publication in a future issue of this journal, but has not been fully edited. Content may change prior to final publication. Citation information: DOI 10.1109/TPWRS.2022.3175933, IEEE Transactions on Power Systems

be regulated to achieve the expected power sharing between microgrid i and microgrid j through η tie lines. The iterative rule for updating the bus voltages of leader DERs in microgrid i is as follows:

$$\boldsymbol{\mathcal{V}}_{(i)}^{G,l} = \boldsymbol{\mathcal{Z}}_{(i,j)} \cdot conj(\frac{\boldsymbol{\mathcal{S}}_{(i,j)}^{In}}{\boldsymbol{\mathcal{V}}_{(j)}^{B}}) + \boldsymbol{\mathcal{V}}_{(j)}^{B} + \tilde{\boldsymbol{\mathcal{V}}}_{(i)}^{G,l} - \tilde{\boldsymbol{\mathcal{V}}}_{(i)}^{B} \quad (1)$$

Here, $\boldsymbol{\mathcal{V}}_{(i)}^{G,l} \in \mathbb{C}^{\eta\times 1}$ denotes the complex bus voltages of η leader DERs corresponding to η tie lines (calligraphic fonts will be used to denote complex numbers); $\boldsymbol{\mathcal{Z}}_{(i,j)} \in \mathbb{C}^{\eta\times\eta}$ denotes the impedance matrix between microgrid i and j with diagonal elements being the impedance of the tie lines; $\boldsymbol{\mathcal{S}}_{(i,j)}^{In} \in \mathbb{C}^{\eta\times 1}$ is the vector of scheduled power injections from microgrid j to i; $\boldsymbol{\mathcal{V}}_{(j)}^{B} \in \mathbb{C}^{\eta\times 1}$ denotes the complex voltages of boundary buses in microgrid j which are connected with microgrid i; $\tilde{\boldsymbol{\mathcal{V}}}_{(i)}^{G,l}$ and $\tilde{\boldsymbol{\mathcal{V}}}_{(i)}^{B}$ are respectively the voltages of leader DER buses and boundary buses in microgrid i at the previous iteration. The rationale behind (1) is that, when a boundary bus's voltage is lower than its target value, a leader DER's bus voltage will be increased following (1), meaning the DER will output more power to increase the voltage profile of the network. The opposite will be performed when the boundary bus voltage is higher than the target value. Such a negative feedback process, if convergent, will achieve the target power interchanges.

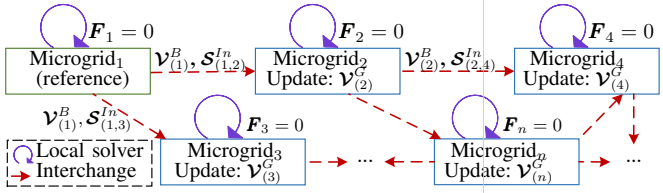

Fig. 2: Outline of PS-APF

Consequently, Fig. 2 presents the outline of the PS-mode APF. An arbitrary DER bus can be chosen as the angle reference in the networked microgrids. The APF procedure starts from microgrid 1, where the reference DER is located. First, the power flow status of microgrid 1 is updated locally with the scheduled power interchanges $\boldsymbol{\mathcal{S}}_{(1,2)}^{In}$ and $\boldsymbol{\mathcal{S}}_{(1,3)}^{In}$ (the local power flow model is detailed in Subsection II-B3). Then, microgrid 1 releases the boundary bus voltages and power interchanges to its neighbors, i.e., microgrid 2 and microgrid 3. Microgrid 2 and 3 therefore update their own power flows independently with their leader DERs' voltages adjusted by (1) to achieve the required boundary conditions. Subsequently, microgrid 4 and microgrid 5 calculate their power flow status separately with the refreshed boundary conditions released by microgrid 2 and microgrid 3. The aforementioned process repeats until all the microgrids are traversed. In the whole procedure, each microgrid interacts with its neighbors using only the boundary information (i.e., boundary bus voltages and tie line powers). Therefore, the local power flow calculation of each individual microgrid is performed distributively and no private information will be disclosed.

[1]The rule of thumb is to choose the leader DER buses to be the ones with the shortest distance from target boundary buses, as this normally leads to faster convergence.

2) Voltage Regulation Mode (VR): The target of VR control mode is to maintain the leader DERs' bus voltages to specific values by adjusting the power injections of the DERs and the power interchanges through tie lines. We observe that, if we solely rely on the power adjustments of the leader DER buses, the power flow calculation may suffer from poor convergence as the scales of microgrids increase. To address this issue, we employ an outer loop for updating the power interchanges on top of the PS mode to achieve voltage restoration.

In our approach, when a leader DER's bus voltage is lower than its rated value, reactive power from the power interchange is increased to support the voltage magnitude. Meanwhile, the active power interchange is reduced to adjust the voltage angle. Similarly, when a leader DER's bus voltage is higher than the rated value, a reversed control logic of power interchange is executed to help the leader DER to restore voltage. The convergence of such a negative feedback loop will realize the target voltage profile. As such, the power interchanges through tie lines are updated as follows:

$$\begin{aligned}\boldsymbol{\mathcal{S}}_{(i,j)}^{In} = &\left(\tilde{\boldsymbol{P}}_{(i,j)}^{In} - \epsilon_p(\boldsymbol{V}_{(i)}^{B} - \boldsymbol{V}_{(i)}^{G,l}\cos\boldsymbol{\theta}_{(i)}^{G,l})\right) \\ &+ j\left(\tilde{\boldsymbol{Q}}_{(i,j)}^{In} + \epsilon_q(\boldsymbol{V}_{i}^{B} - \boldsymbol{V}_{(i)}^{G,l}\sin\boldsymbol{\theta}_{(i)}^{G,l})\right)\end{aligned} \quad (2)$$

Here, $\boldsymbol{P}_{(i,j)}^{In} = \mathrm{Re}(\boldsymbol{\mathcal{S}}_{(i,j)}^{In})$ and $\boldsymbol{Q}_{(i,j)}^{In} = \mathrm{Im}(\boldsymbol{\mathcal{S}}_{(i,j)}^{In})$ respectively denote the active and reactive power injections through tie lines from microgrid i to j; $\tilde{\boldsymbol{P}}_{(i,j)}^{In}$ and $\tilde{\boldsymbol{Q}}_{(i,j)}^{In}$ respectively denote the values of $\boldsymbol{P}_{(i,j)}^{In}$ and $\boldsymbol{Q}_{(i,j)}^{In}$ inherit from the previous iteration; $\boldsymbol{V}_{(i)}^{G,l} = |\boldsymbol{\mathcal{V}}_{(i)}^{G,l}|$ and $\boldsymbol{\theta}_{(i)}^{G,l} = \arg(\boldsymbol{\mathcal{V}}_{(i)}^{G,l})$ respectively denote the voltage amplitudes and angles of the leader DER buses; ϵ_p and ϵ_q are step sizes for updating real and reactive power. Proper values of ϵ_p and ϵ_q can be set as the real and imaginary parts of $\boldsymbol{S}^{Ls}/\boldsymbol{V}_{base}$ in a local microgrid, where $\boldsymbol{S}^{Ls}$ is the total load consumption, $\boldsymbol{V}_{base}$ is the base voltage. In this circumstance, a faster convergence is achieved for the VR outer loop.

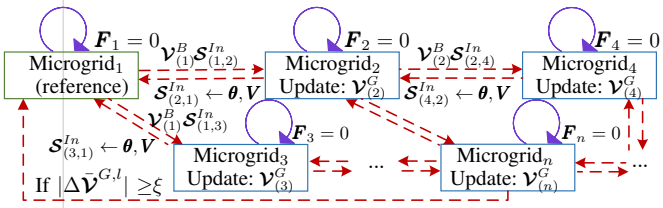

Fig. 3: Outline of VR-APF

The outline of the VR-mode APF is established in Fig. 3. First, power flow status of networked microgrids are initialized by PS-APF with power interchanges $\boldsymbol{\mathcal{S}}_{(i,j)}^{In}$ scheduled as zero. Then, the power interchanges are adjusted according to (2) to achieve the target voltages of leader DERs within each microgrid. Next, each microgrid update the local power flow by PS-APF with the refreshed power interchanges. Aforementioned VR procedure continues until the leader DERs' voltages recover to nominal values $\boldsymbol{\mathcal{V}}^{G,l^*}$, which indicates $|\Delta\bar{\boldsymbol{\mathcal{V}}}^{G,l}| = |\boldsymbol{\mathcal{V}}^{G,l^*} - \boldsymbol{\mathcal{V}}^{G,l}| \leq \xi$.

3) Distributed Power Flow Formulation of Each Microgrid: The following establishes the distributed power flow model of each microgrid with a thorough formulation of hierarchical

This article has been accepted for publication in a future issue of this journal, but has not been fully edited. Content may change prior to final publication. Citation information: DOI 10.1109/TPWRS.2022.3175933, IEEE Transactions on Power Systems

control. Without loss of generality, we study the distributed power flow formulation of an arbitrary microgrid i. Denote the number of buses, DERs and leader DERs as N, n and n_l. Denote the power interchanges between microgrid i and all its neighboring microgrids as $\boldsymbol{\mathcal{S}}^{In}$. Here, $\boldsymbol{\mathcal{S}}^{In}$ is modelled as a vector so that APF is capable of handling power sharing among multiple tie lines.

The active power sharing among DERs in microgrid i follows the hierarchical control logic as:

$$f - f_k^{ref} = -\alpha_k^G (P_k^G - P_k^{ref} + \Omega_k^G) \tag{3}$$

Here, f denotes the frequency of the networked microgrid, which will be adjusted to achieve the nominal frequency f^* (i.e., 60Hz) via hierarchical control of all microgrids; f_k^{ref} denotes the reference frequency signal of DER k; α_k^G denotes the P/f droop coefficient of DER k; P_k^G and P_k^{ref} respectively denote the active power generation and the reference active power of DER k; Ω_k^G denotes the secondary control signal for frequency regulation. Specifically, the follower DERs jointly share a frequency unbalance amount $\hat{f}$ according to their droop coefficients to assist frequency recovery:

$$\Omega_k^G = \hat{f}/\alpha_k^G \quad , \quad k \in \mathbb{S}_f^G \tag{4}$$

where $\mathbb{S}_f^G$ denotes the set of follower DERs.

Integrating (3) and (4) yields the active power characteristics of *DER buses*:

$$\boldsymbol{P}^G = \boldsymbol{P}^{ref} - \frac{1}{\boldsymbol{\alpha}^G}\left(f^* - \boldsymbol{f}^{ref}\right) - \boldsymbol{\Omega}^G = \begin{cases} P_k^G(\Omega_k^G), k \in \mathbb{S}_l^G \\ P_k^G(\hat{f}), k \in \mathbb{S}_f^G \end{cases} \tag{5}$$

where $\boldsymbol{P}^G$, $\boldsymbol{P}^{ref}$, $\boldsymbol{\alpha}^G$, $\boldsymbol{f}^{ref}$, $\boldsymbol{\Omega}^G \in \mathbb{R}^{n\times 1}$ are respectively the vector forms of the corresponding variables; $\mathbb{S}_l^G$ denotes the set of leader DERs.

For reactive power sharing, leader DERs adopt hierarchical control (see (6)) to achieve the scheduled $\boldsymbol{V}^G$, while follower DERs adopt droop control (see (7)) to assist leader DERs:

$$V_k^{G,l} - V_k^{ref} = -\beta_k^G (Q_k^G - Q_k^{ref}) - e_k^G \quad , \ k \in \mathbb{S}_l^G \tag{6}$$

$$V_k^G - V_k^{ref} = -\beta_k^G (Q_k^G - Q_k^{ref}) \quad , \ k \in \mathbb{S}_f^G \tag{7}$$

where $V_k^{G,l}$ is the target bus voltage of leader DER k pre-determined by the PS/VR mode as detailed in Subsections II-B1 and II-B2; V_k^G and V_k^{ref} respectively denote the voltage amplitude of DER k and its reference value; β_k^G denotes the Q/V droop coefficient; Q_k^G and Q_k^{ref} respectively denote the reactive power generation and its reference value; e_k^G denotes the secondary control signal for voltage regulation.

Integrating (6) and (7) leads to a unified formulation of the reactive power characteristics of *DER buses*:

$$\boldsymbol{Q}^G(\hat{\boldsymbol{V}}^G) = \boldsymbol{Q}^{ref} - \frac{1}{\boldsymbol{\beta}^G}\left(\boldsymbol{V}^* - \boldsymbol{V}^{ref} + \hat{\boldsymbol{V}}^G\right) \tag{8}$$

Here, $\boldsymbol{Q}^G, \boldsymbol{Q}^{ref}, \boldsymbol{\beta}^G, \boldsymbol{V}^{ref} \in \mathbb{R}^{n\times 1}$ are respectively the vector forms of the corresponding variables; $\hat{\boldsymbol{V}}^G \in \mathbb{R}^{n\times 1}$ and $\boldsymbol{V}^* \in \mathbb{R}^{n\times 1}$ are defined as follows:

$$\hat{\boldsymbol{V}}^G = \begin{cases} e_k^G & , \ k \in \mathbb{S}_l^G \\ V_k^G & , \ k \in \mathbb{S}_f^G \end{cases}, \quad \boldsymbol{V}^* = \begin{cases} V_k^{G,l} & , \ k \in \mathbb{S}_l^G \\ 0 & , \ k \in \mathbb{S}_f^G \end{cases}$$

Subsequently, the summation of DER power generations are derived based on (5) and (8):

$$P^{Gs} = \sum\nolimits_k (P_k^{ref} + \frac{f_k^{ref}}{\alpha_k^G}) - (\sum\nolimits_k \frac{1}{\alpha_k^G})(f^* + \hat{f}) \tag{9}$$

$$Q^{Gs} = \sum\nolimits_k Q_k^{ref} - \sum\nolimits_k \frac{1}{\beta_k^G}(V_k^* - V_k^{ref} + \hat{V}_k^G) \tag{10}$$

With the formulation of DER buses, the following power flow states are to be solved for microgrid i:

- $\hat{\boldsymbol{\theta}} \in \mathbb{R}^{(N-n_l)\times 1}$ assembling the voltage angles of non-leader-DER buses[2];
- $\hat{\boldsymbol{V}} \in \mathbb{R}^{N\times 1}$ assembling the voltage amplitudes of non-DER buses and $\hat{\boldsymbol{V}}^G$ of DER buses (see (8));
- $\hat{f}$ denoting the frequency unbalance variable defined in (4).

To achieve the voltage angles $\arg(\boldsymbol{\mathcal{V}}_{(i)}^{G,l})$ determined by the PS/VR regulation (see (1)), we let the leader DERs adjust their active power outputs freely with (9) still holds. Therefore, Ω_k^G for $k \in \mathbb{S}_l^G$ need not to be involved in power flow calculation.

Consequently, we establish the APF power flow formulation of microgrid i as follows:

$$\boldsymbol{F}_i(\hat{\boldsymbol{\theta}}, \hat{\boldsymbol{V}}, \hat{f}) = \begin{bmatrix} \boldsymbol{\phi}^{nl} \cdot \boldsymbol{P}^G - \boldsymbol{P}^L - \boldsymbol{Y}_p \cdot \boldsymbol{V}_b \circ \boldsymbol{V}_b - \boldsymbol{P}^{In} \\ \boldsymbol{\phi}^{nr} \cdot \boldsymbol{Q}^G - \boldsymbol{Q}^L - \boldsymbol{Y}_q \cdot \boldsymbol{V}_b \circ \boldsymbol{V}_b - \boldsymbol{Q}^{In} \\ P^{Gs} - P^{Ls} - P^{Ins} - P^{loss} \\ Q^{Gs} - Q^{Ls} - Q^{Ins} - Q^{loss} \end{bmatrix} = \boldsymbol{0} \tag{11}$$

In (11), the first and second row blocks respectively formulate the nodal active power balance at non-leader-DER buses and nodal reactive power balance at non-reference buses, where $\boldsymbol{\phi}^{nl} \in \mathbb{R}^{(N-n)\times n}$ is the incidence matrix between non-leader-DER buses and DERs, whose (k,j)-element is 1 when DER j is connected to a non-leader-DER bus j, and 0 otherwise; $\boldsymbol{\phi}^{nr} \in \mathbb{R}^{(N-1)\times n}$ is the incidence matrix between non-reference buses and DERs; $\boldsymbol{P}^L$ and $\boldsymbol{P}^{In}$ respectively denote the active power loads and power interchanges at non-leader-DER buses; $\boldsymbol{Q}^L$ and $\boldsymbol{Q}^{In}$ respectively denote the reactive power loads and power interchanges at non-reference buses; $\boldsymbol{Y}_p$ and $\boldsymbol{Y}_q$ denote the modified admittance matrices [3]; $\boldsymbol{V}_b$ denotes the bus voltage amplitudes. The last two row blocks in (11) respectively formulate the active and reactive power balance in microgrid i, where P^{Gs}, P^{Ls}, P^{Ins} and P^{loss} respectively denote the total active power generations, loads, power interchanges and loses; similarly, Q^{Gs}, Q^{Ls}, Q^{Ins} and Q^{loss} respectively denote the reactive components.

With the distributed APF model of each microgrid, we summarize the PS/VR-based procedure at a high level:

- In the PS mode, the power interchange $\boldsymbol{\mathcal{S}}_{(i,j)}^{In}$ is scheduled. APF first refreshes $\boldsymbol{\mathcal{V}}^{G,l}$ based on (1). Then, power flows of each individual microgrid, i.e., $\boldsymbol{F}_i = \boldsymbol{0}(\forall i)$ in (11), are

[2]Note that voltage angles of leader-DER buses are pre-determined by the PS/VR regulation (see Subsections II-B1 and II-B2)

[3]$\boldsymbol{Y}_p$ and $\boldsymbol{Y}_q$ are the modified admittance matrices of microgrid i:

$$\begin{cases} Y_{p,kl} = |Y_{kl}|cos(\theta_k - \theta_l - \delta_{kl}) \ , \ \forall k,l \\ Y_{q,kl} = |Y_{kl}|sin(\theta_k - \theta_l - \delta_{kl}) \ , \ \forall k,l \end{cases} \tag{12}$$

where Y_{kl} and δ_{kl} are the admittance magnitude and angle of branch k-l.

solved. The Newton-Raphson iteration is applied here until the errors in $\hat{\boldsymbol{\theta}}, \hat{\boldsymbol{V}}, \hat{f}$ reach the tolerance ξ:

$$\Delta \boldsymbol{F}_i(\hat{\boldsymbol{\theta}}, \hat{\boldsymbol{V}}, \hat{f}) = \boldsymbol{J}_i \cdot \left[\Delta\hat{\boldsymbol{\theta}}, \Delta\hat{\boldsymbol{V}}, \Delta\hat{f}\right]^T \tag{13}$$

where $\boldsymbol{J}_i$ denotes the Jacobian matrices of the APF model. Due to page limitation, details of $\boldsymbol{J}_i$ are omitted.

- In the VR mode, the power interchange $\boldsymbol{S}_{i,j}^{In}$ is updated based on (2) at first. Then, $\boldsymbol{V}_i^G$ is refreshed based on (1), followed by the power flow calculation of each individual microgrid based on (11). The APF calculation continues until the bus voltages reach the target values.

C. APF Extension to DC Microgrid

So far the aforementioned APF formulation discusses AC microgrids by default. Nevertheless, it can be readily extended to hybrid AC/DC networked microgrids. This subsection establishes the hierarchical-controlled DC microgrid formulation for APF study.

In a DC microgrid i_{dc}, denote the voltage amplitude of DER bus k as V_k^D and the active power generation as P_k^D. If DER k adopts primary control, it will meet the power demand at a cost of local voltage deviation:

$$P_k^D(V_k^D) = \frac{1}{\gamma_k^D}(V_k^{D,ref} - V_k^D) + P_k^{D,ref} \tag{14}$$

where γ_k^D is the droop coefficient of DER k; $V_k^{D,ref}$ and $P_k^{D,ref}$ are respectively the reference voltage and power.

If DER k adopts secondary control, it will coordinate with other DERs to recover DC bus voltages by a further power dispatch. Here, we design dummy buses which can adjust the DER power injections to achieve voltage restoration:

$$P_k^D(V_k^D) = V_k^D Y_k^s (V_k^s + V_k^{D,*} - 2V_k^D) + P_k^{D,ref} \tag{15}$$

where V_k^s denotes the voltage amplitude of the dummy bus corresponding to DER k; Y_k^s the denotes the virtual conductance between dummy bus V_k^s and DER bus V_k^D; $V_k^{D,*}$ represents the rated bus voltages. In APF calculation, V_k^s is updated as $V_k^s = \tilde{V}_k^s + V_k^{D,*} - 2V_k^D$ [40], [41] at each iteration until convergence (i.e., $\tilde{V}_k^s$ denotes the value of V_k^s at the previous iteration).

Specifically, interlinking converters are implemented between AC and DC microgrids to balance the overall power consumption in the networked microgrid [22]. V/ω droop control is adopted at the interlinking converter to alleviate load mismatches between DC microgrid i_{dc} and its neighboring AC microgrids [22]:

$$P_k^{IC}(V_k^{IC}) = \frac{1}{\gamma_k^{IC}}(\varrho_\omega \omega - \varrho_v V_k^{IC} + \varrho_0) \tag{16}$$

where, γ_k^{IC} is the droop coefficient of interlinking converter k; ω is the angle frequency; V_k^{IC} is the bus voltage of the interlinking converter; $\varrho_\omega, \varrho_v, \varrho_0$ are control coefficients.

Consequently, the power flow model of DC microgrid i_{dc} is formulated as:

$$\boldsymbol{F}_{i_{dc}}(\boldsymbol{V}_d) = \left[\boldsymbol{\phi}^D \boldsymbol{P}^D - \boldsymbol{\phi}^{IC} \boldsymbol{P}^{IC} - \boldsymbol{P}_d^L - \bar{\boldsymbol{Y}}_d \cdot \boldsymbol{V}_d \circ \boldsymbol{V}_d\right] \tag{17}$$

where $\boldsymbol{P}_d^L$ and $\boldsymbol{P}^IC$ are respectively the DERs outputs, DC loads and power interchange with neighboring AC microgrids; $\boldsymbol{\phi}^D$ and $\boldsymbol{\phi}^{IC}$ are the corresponding incidence matrices between buses; $\boldsymbol{V}_d$ denotes bus voltages of DC microgrid i_{dc}; $\boldsymbol{P}^D$, $\bar{\boldsymbol{Y}}_d$ is the DC conductance matrix.

The distributed APF procedure of hybrid AC/DC networked microgrids is therefore established as follows. After finishing the APF calculation of each DC microgrid individually, boundary bus voltages will be transferred to the interconnected AC microgrids to initiate the independent APF calculation for each AC microgrid. The whole process repeats until boundary bus voltages converge.

III. APF-based Continuation Power Flow

In this section, an APF-based continuation power flow algorithm (CPF$^+$) is further developed to facilitate steady-state voltage stability analysis of networked microgrids under various hierarchical control modes. The CPF$^+$ algorithm is again established in a fully distributed manner to support the plug-and-play and privacy preserving in networked microgrids.

A. CPF$^+$ Methodology

Without loss of generality, we consider droop coefficients and power interchanges as the influencing factors λ. The power changes can be simulated by:

$$\begin{cases} \boldsymbol{P}^G(\lambda_1) = \boldsymbol{P}^{ref} - \frac{1}{(1+\lambda_1)\boldsymbol{\alpha}^G}\left(f^* - \boldsymbol{f}^{ref}\right) - \boldsymbol{\Omega}^G \\ \boldsymbol{Q}^G(\lambda_1) = \boldsymbol{Q}^{ref} - \frac{1}{(1+\lambda_1)\boldsymbol{\beta}^G}\left(\boldsymbol{V}^* - \boldsymbol{V}^{ref} + \hat{\boldsymbol{V}}^G\right) \end{cases} \tag{18}$$

$$\begin{cases} \boldsymbol{P}^{In}(\lambda_2) = \boldsymbol{P}_0^{In} + \lambda_2(S_{base} cos\varphi_{Li}) \\ \boldsymbol{Q}^{In}(\lambda_2) = \boldsymbol{Q}_0^{In} + \lambda_2(S_{base} sin\varphi_{Li}) \end{cases} \tag{19}$$

where $\boldsymbol{P}_0^{In}$ and $\boldsymbol{Q}_0^{In}$ are the original real powers and reactive powers flowing through tie lines; S_{base} is the power base; φ_{Li} is the power factor angle of tie line flow.

As presented in Fig. 4, CPF$^+$ consists of a predictor and a corrector, both implemented distributedly. The predictor and the corrector jointly solve the power flow of networked microgrids with successively increased impact factors (i.e., droop coefficients or microgrid power interchanges) until the critical point is reached, which indicates a voltage collapse of the networked microgrids.

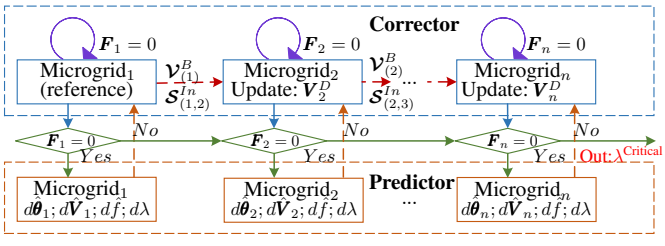

Fig. 4: Outline of CPF$^+$

The predictor step is used to provide an approximate point when the specified factors change to the next step. The prediction can be calculated by choosing a non-zero value for one of the components of the tangent vector, as follows

$$\begin{bmatrix} \frac{\partial \boldsymbol{F}_i}{\partial \hat{\boldsymbol{\theta}}} & \frac{\partial \boldsymbol{F}_i}{\partial \hat{\boldsymbol{V}}} & \frac{\partial \boldsymbol{F}_i}{\partial \hat{f}} & \frac{\partial \boldsymbol{F}_i}{\partial \lambda} \\ \mathbf{0} & \mathbf{0} & \mathbf{0} & 1 \end{bmatrix} \begin{bmatrix} d\hat{\boldsymbol{\theta}} \\ d\hat{\boldsymbol{V}} \\ d\hat{f} \\ d\lambda \end{bmatrix} = \begin{bmatrix} \mathbf{0} \\ \pm 1 \end{bmatrix} \tag{20}$$

where $\lambda \in \{\lambda_1, \lambda_2\}$. Once the tangent vector is obtained by solving (20), the prediction can be made as follows,

$$[\hat{\boldsymbol{\theta}}; \hat{\boldsymbol{V}}; \hat{f}; \lambda] + \epsilon [d\hat{\boldsymbol{\theta}}; d\hat{\boldsymbol{V}}; d\hat{f}; d\lambda] \longrightarrow [\hat{\boldsymbol{\theta}}; \hat{\boldsymbol{V}}; \hat{f}; \lambda] \tag{21}$$

where ϵ is the predictor step size.

The corrector step aims to calculate APF with the predicted initial values. It first updates the droop coefficient or power interchange and then calculates voltages. For instance, if the goal is to identify the safe operating region of droop coefficients, the i^{th} microgrid's variables can be calculated by solving the following equation

$$\Delta \boldsymbol{F}_i(\hat{\boldsymbol{\theta}}; \hat{\boldsymbol{V}}; \hat{f}; \lambda_1) = \boldsymbol{J}_i \cdot \left[\Delta \hat{\boldsymbol{\theta}}; \Delta \hat{\boldsymbol{V}}; \Delta \hat{f}; \Delta \lambda_1\right]^T \tag{22}$$

If the goal is to pinpoint feasible power interchanges, a distributed APF framework can be exploited to perform a traversal of power interchanges among microgrids.

B. Distributed APF-CPF$^+$ Framework

A distributed framework with a triple loop process is developed for both APF and CPF$^+$ algorithms, mainly for the purposes of scalability and privacy-preserving. Algorithm 1 summarizes the framework.

Algorithm 1: An Integrative APF-CPF$^+$ Algorithm

Initialize: $\hat{\boldsymbol{\theta}}$,$\hat{\boldsymbol{V}}$,$\hat{f}$, $\boldsymbol{\mathcal{V}}^{G,l}$, $\boldsymbol{\mathcal{S}}^{In}$, ξ, $\boldsymbol{V}^s$, $\boldsymbol{V}_d$, $\boldsymbol{Y}_d$, λ ;
while $|\Delta \bar{\boldsymbol{\mathcal{V}}}^{G,l}| \geq \xi$ **do**
  Update: Predictor **Eq.** (20, 21) ;
  while $\Delta \boldsymbol{\mathcal{V}}^{G,l} \geq \xi$ **do**
    while $\Delta\hat{\boldsymbol{\theta}}$, $\Delta\hat{\boldsymbol{V}}$, $\Delta\hat{f}$, $\Delta \boldsymbol{V}^s$, $\Delta \boldsymbol{V}_d \geq \xi$ **do**
      if *DER bus or boundary bus* **then**
        Update: $\boldsymbol{P}^G$, $\boldsymbol{Q}^G$,P^{Gs}, Q^{Gs}, $\boldsymbol{P}^D$, $\boldsymbol{P}^{IC}$, $\boldsymbol{P}^G(\lambda)$, $\boldsymbol{Q}^G(\lambda)$, $\boldsymbol{P}^{In}(\lambda)$, $\boldsymbol{Q}^{In}(\lambda)$, $\boldsymbol{F}_i$, $\boldsymbol{F}_{i_{dc}}$ **Eq.**(5, 8-11, 14-19);
      else
        Update: $\boldsymbol{F}_i$, $\boldsymbol{F}_{i_{dc}}$ **Eq.** (11, 17);
      end
      Update: $\Delta\hat{\boldsymbol{\theta}}$, $\Delta\hat{\boldsymbol{V}}$, $\Delta\hat{f}$, $\boldsymbol{V}^s$, $\Delta \boldsymbol{V}_d$, $\boldsymbol{J}_i$, $\boldsymbol{J}_{i_{dc}}$ **Eq.**(13, 22);
      Update: $\hat{\boldsymbol{\theta}}$, $\hat{\boldsymbol{V}}$, $\hat{f}$, $\boldsymbol{V}_d$;
    end
    Update:$\boldsymbol{\mathcal{V}}^{G,l}$ **Eq.** (1);
  end
  Update: $\boldsymbol{\mathcal{S}}^{In}$, $\boldsymbol{P}^{In}(\lambda)$, $\boldsymbol{Q}^{In}(\lambda)$ **Eq.** (2, 19);
end
Result: $\hat{\boldsymbol{\theta}}$,$\hat{\boldsymbol{V}}$,$\hat{f}$, $\boldsymbol{\mathcal{V}}^{G,l}$, $\boldsymbol{V}_d$ λ.

1) *Tertiary loop* is to achieve VR control objectives. The VR mode modifies power injections based on (2) to facilitate DER bus voltages recover to nominal values.

2) *Secondary loop* updates bus voltages of leader DERs and thus regulating power interchanges through multiple tie lines to realize PS mode. Once power interchanges $\boldsymbol{\mathcal{S}}^{In}$ are scheduled, boundary bus voltages will be tuned to the target values by adjusting leader DER buses based on (1). Whereas, when it comes to the continuation algorithm for searching the interface power margin, power interchanges with increasing factor are integrated into the PS mode, and the secondary loop continues until the critical point is reached. The continuation process for traversing droop coefficients keeps the power interchanges constant during each iteration of the secondary loop.

3) *Primary loop* is to update voltage profiles of networked microgrids, which performs distributed APF computations for the individual microgrids. The power flow solver of each microgrid calculates the power flow states locally. Microgrids exchange only boundary bus information with the neighbouring microgrids. The computing sequence is as follows. The power flow of microgrid i that contains angle reference bus is required to be calculated first. (1) If microgrid i is connected with DC microgrids, its frequency f will be passed to the DC microgrids. Once the DC microgrid power flow with droop and/or secondary controls converges, the boundary bus voltages $\boldsymbol{V}_d$ will be passed on to update microgrid i's power flows; (2) If microgrid i is connected with neighbouring AC microgrid j, the boundary bus voltages $\boldsymbol{V}^B_{(i)}$ will be passed on to the neighbouring AC microgrid. Then, target voltages for boundary buses in microgrid j can be scheduled. Subsequently, once power interchange $\boldsymbol{\mathcal{S}}^{In}_{(i,j)}$ and leader bus voltages $\boldsymbol{\mathcal{V}}^{G,l}_{(j)}$ are updated, power flows of the neighbouring microgrid j can be solved based on its own power flow solver. CPF$^+$ with droop coefficients and power interchange scanning shares the same primary loop procedures.

The aforemetioned distributed APF-CPF$^+$ platform is both programmable and secure in that

- Jacobian matrices of all microgrids are updated separately and flexibly, fully supporting plug-and-play of microgrids and microgrid components.
- Various hierarchical control modes [39] of networked microgrids can be programmed in APF's outer loop/inner loop, and the switching of control modes can be readily simulated in APF and CPF$^+$.
- Only boundary buses data (e.g., voltages and interface flows through tie lines) need to be shared with neighboring microgrids, which can protect the local customers' privacy.

IV. Numerical Tests

Extensive case studies are performed to verify the efficacy of APF and CPF$^+$. All codes are implemented in MATLAB 2018a on a 2.50 GHz PC. Dynamic verification is performed using a Real-Time Digital Simulator (RTDS™).

A. Validity and Accuracy of APF

First of all, a high-fidelity RTDS model for a two-microgrid, 14-bus test system (see Fig. 5) is built to validate the correctness of APF. By flipping the normally-open switch, a microgrid configuration can be toggled from islanded to connected mode. Table I presents the component and control parameters of the test system. Table II compares the APF results under different controls with the RTDS time-domain simulation

This article has been accepted for publication in a future issue of this journal, but has not been fully edited. Content may change prior to final publication. Citation information: DOI 10.1109/TPWRS.2022.3175933, IEEE Transactions on Power Systems

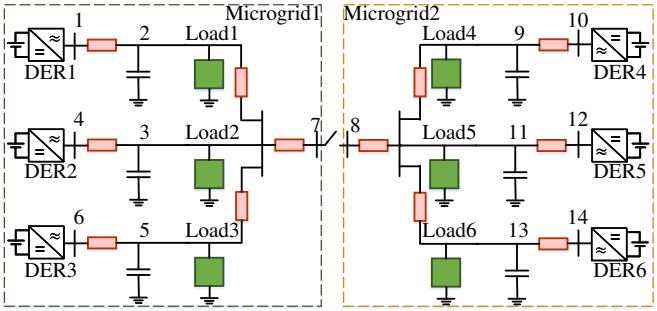

Fig. 5: A two-microgrid, 14-bus test system. Base voltage: 179.4 V. Base power: 60kVA. The P/f droop coefficients for DERs {1,3,4,6} and {2,5} are defined as 6e-6 and 1.2e-6, respectively. The corresponding Q/V droop coefficients are set as 1.2e-3 and 3e-3, respectively.

TABLE I: Parameters of the two-microgrid, 14-bus test system

Parameters	Values
Base voltage	179.4 V
Base power	60kVA
DC source initial values	0.4kV
Active power of loads in PQ buses {1,3,4,6}	10kW
Reactive power of loads in PQ buses {1,3,4,6}	5kVar
Active power of loads in PQ buses{2,5}	5kW
Reactive power of loads in PQ buses{2,5}	2kVar
P/f droop coefficients for DERs {1,3,4,6}	6e-6
P/f droop coefficients for DERs {2,5}	1.2e-6
Q/V droop coefficients for DERs {1,3,4,6}	1.2e-3
Q/V droop coefficients for DERs {2,5}	3e-3
Resistance of the lines	0.1Ohm
Reactance of the lines	1.35e-3H

results in steady-state, in which the maximum error rate (er) is found to be less than 0.07%. Fig. 6 compares the dynamic voltage process of bus 2 (see the blue trajectory) under four events with the steady-state APF solutions (see the red dotted curve) during the four events. At 15s, Loads 1 and 3 are increased from 0.1666+j0.0833 p.u. to 0.2+j0.1083 p.u. under droop controls only. Further, they are reduced to 0.2+j0.1p.u. at 23s. Then, Microgrids 1 and 2 are interconnected at 27s and DER 2 is changed to the VR mode. Finally, the PS mode is switched on at 42s. The agreement of RTDS and APF results assuredly validate the correctness of APF.

TABLE II: Voltage profiles and frequency under different controls(p.u.)

Method		APF			RTDS		
MG	Bus	Droop [1]	PS [2]	VR [2]	Droop	PS	VR
1	1	0.9865	1.0425	1.0173	0.9864	1.0421	1.0171
	2	0.8429	0.9096	0.8831	0.8431	0.9091	0.8827
	3	0.8657	0.9302	0.9071	0.8663	0.9299	0.9075
	4	0.9637	1.0203	1.0000	0.9632	1.0197	0.9999
	5	0.8429	0.9096	0.8831	0.8431	0.9091	0.8827
	6	0.9865	1.0425	1.0173	0.9864	1.0421	1.0171
	7	0.8657	0.9276	0.9120	0.8663	0.9276	0.9126
Frequency		0.9998	1	1	0.9998	1	1
2	8	0.8954	0.9252	0.9169	0.8959	0.9253	0.9176
	9	0.8798	0.9063	0.9086	0.8801	0.9059	0.9089
	10	0.9947	1.0158	1.0210	0.9946	1.0152	1.0208
	11	0.8954	0.9227	0.9221	0.8959	0.9231	0.9228
	12	0.9753	0.9998	1.0000	0.9749	0.9993	1.0000
	13	0.8798	0.9063	0.9086	0.8801	0.9059	0.9089
	14	0.9947	1.0158	1.0210	0.9946	1.0152	1.0207
Frequency		0.9999	1	1	0.9999	1	1

[1] Droop-based networked microgrids are validated by opening the switch.
[2] PS/VR-based power flows are verified by interconnecting 2 microgrids.

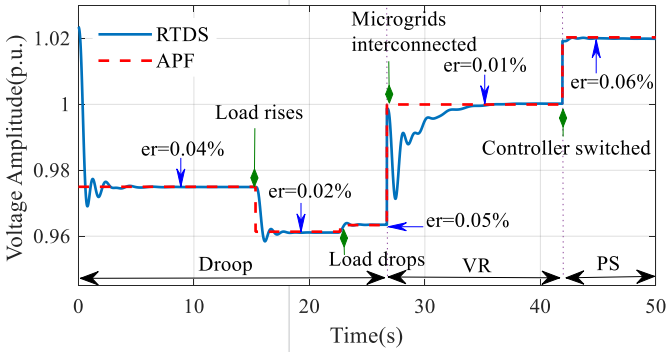

Fig. 6: Comparison between APF and RTDS results

B. Efficacy and Versatility of APF

In the following subsections, we study the performance of APF and CPF$^+$ using an eight-microgrid test system. The efficacy and versatility of the devised methods (see this subsection), the convergence performance (see subsection V.C), CPF$^+$-based static voltage stability operating region (see subsection V.D) and APF-based networked microgrid reconfiguration (see subsection V.E) will be thoroughly evaluated.

As illustrated in Fig. 7, the eight-microgrid test system is established by interlinking and modifying the low voltage network of the IEEE 342-bus distribution system [42] into networked microgrids which consist of 4 meshed AC microgrids (Microgrids 1, 3, 4 and 6), 2 radial AC microgrids (Microgrid 2 and 5) and 2 DC microgrids (Microgrid 7 and 8). Table III shows the droop coefficients of DERs in the test system. Detailed parameters of lines and loads in AC microgrids are listed in Tables VIII and IX in Appendix, respectively. The parameters of DC microgrids can be found in [17], [21].

TABLE III: Droop coefficients of DERs in the eight-microgrid system (p.u.)

Bus	4	45	28	42	27	11	9	14
m/n	1	1	1	1	0.8	0.8	1	1
Bus	24	50	54	18	59	36	30	109
m/n	1	1	1	0.8	1	1	1	1
Bus	83	86	110	126	132	137	91	96
m/n	1	1.5	0.9	1	1	1.2	1.5	0.8
Bus	111	107	118	101	140	144		
m/n	1	1	1	1	1	1		
Bus	157	159	169	170	148	152		
k	0.5	0.4	0.6489	0.6489	0.5	0.4		

m: P/f droop coefficients in AC microgrids. **n**: Q/V droop coefficients in AC microgrids. **k**: P/V droop coefficients in DC microgrids.

This subsection investigates networked microgrid power flow under various control modes and different system structures via APF.

1) APF Results under Droop Control: We first validate the droop-based networked microgrid operations by opening all the switches. Table IV presents the microgrid frequency and power outputs of partial DERs in Microgrids 1, 2, 3 and Microgrid 8.

The simulation results show that the generation and demand in each microgrid are balanced at a cost of deviated frequency and voltages. For example, the system frequency drops down to 0.9971 p.u. in microgrid 3 when DERs boost real power

This article has been accepted for publication in a future issue of this journal, but has not been fully edited. Content may change prior to final publication. Citation information: DOI 10.1109/TPWRS.2022.3175933, IEEE Transactions on Power Systems

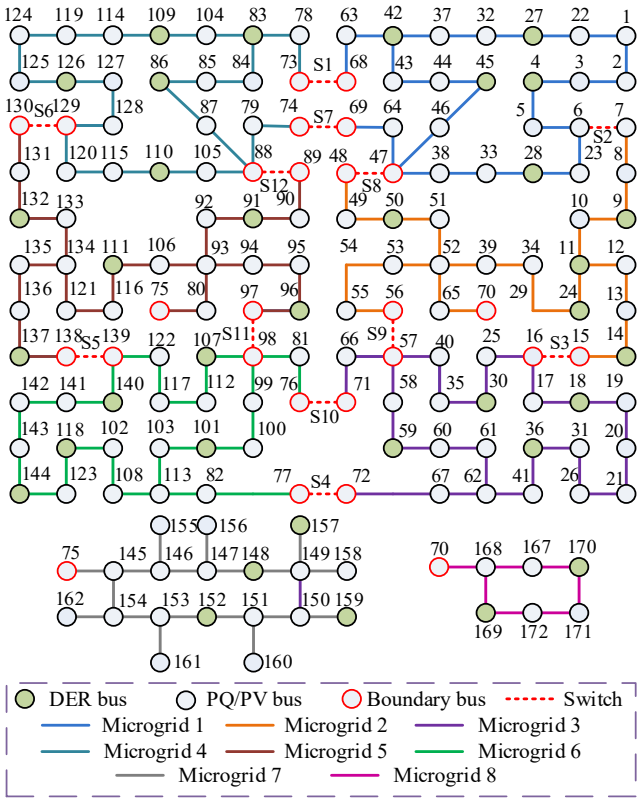

Fig. 7: An eight-microgrid test system. Base voltage: 120 V. Base power: 5.15MVA.

injections to support loads and line losses (See Table IV). The voltage of bus 59 is decreased to 0.9966 p.u. for the increase of reactive power injections. The voltage of bus 170 declines to 0.998 p.u. to balance the active power consumption. The P/f and Q/V droop characteristics enable local microgrids to balance the power mismatches when each microgrid operates autonomously.

TABLE IV: DER adjustments under droop control

MG	Bus	Power of DERs	Initial Power of DERs	Bus voltage	Microgrid frequency
1	4	0.0281+j0.0217	0.0276+j0.0169	0.9952	0.9995
	28	0.0281+j0.0195	0.0276+j0.0169	0.9974	
	45	0.0281+j0.0173	0.0276+j0.0169	0.9996	
2	11	0.0399+j0.0162	0.0388+j0.0194	1.0026	0.9991
	14	0.0203+j0.0114	0.0194+j0.0117	1.0002	
	24	0.0203+j0.0054	0.0194+j0.0058	1.0004	
3	59	0.0363+j0.0208	0.0334+j0.0175	0.9966	0.9971
	18	0.0350+j0.0264	0.0276+j0.0233	0.9976	
	36	0.0330+j0.0248	0.0276+j0.0194	0.9946	
8	169	0.0017	0	0.9989	-
	170	0.0031	0	0.9980	

2) APF Results under PS Control: Under PS control, we interconnect those 8 microgrids by closing all switches. To validate the capability of PS-based APF to maintain boundary buses' voltages, 100 stochastic scenarios are generated with randomized power loads in microgrid 1 and 3.

Fig. 8 compares the voltage amplitudes under PS control and droop control. It can be observed from Fig. 8(a) that when neighboring microgrids are interconnected, PS-based

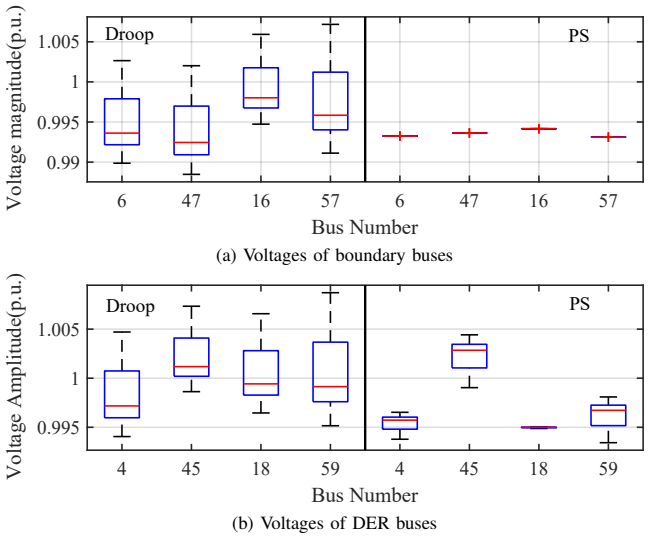

(a) Voltages of boundary buses

(b) Voltages of DER buses

Fig. 8: Comparison of bus voltage amplitudes: droop control vs PS control

APF can adjust local boundary buses' voltages to achieve scheduled power interchanges. For example, the boundary bus 6 can always remain at 0.9932 p.u. under PS mode, regardless of how the local power consumption changes. In contrast, under droop control, the voltage of boundary buses can not be maintained. The voltage amplitudes of DER buses in Fig. 8(b) also show that the PS mode has a less effect on voltage variations of DER buses. For example, the voltage variation of bus 4 under the PS mode is smaller than that under droop control. Meanwhile, the voltage variation of bus 18 is smaller than other DER buses because of smaller droop coefficients.

Further, Fig. 9 presents the voltage profiles under different power interchanges. Those results indicate that PS control can effectively relieve power deficiencies in individual microgrids during a utility side outage. For example, when Microgrid 2 requests for extra power ($\boldsymbol{S}^{In} = 0.0086 + j0.0056 p.u.$) from neighboring microgrids, Microgrids 1 and 3 can boost boundary buses' voltages to transfer the scheduled power interchanges in Fig. 9.

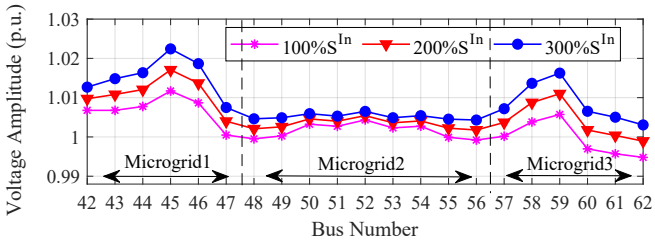

Fig. 9: PS-APF voltage profiles under different power interchanges

3) APF Results under VR Control: Fig. 10 illustrates the efficacy of APF under VR control. Simulation results prove that under the VR mode, the leader DER voltages can be recovered to the nominal values through the coordination of power interchange between microgrids. For example, bus 4's voltage in Fig. 10(a) is adjusted to the nominal value by regulating the tie line S2 power to -0.0035+0.0056i p.u.. DER buses in DC microgrids also reach the nominal values, such as voltages at buses 169 and 170 in Microgrid 8 (see Fig. 10(b)). Table V compares the voltages in VR-based, interconnected

This article has been accepted for publication in a future issue of this journal, but has not been fully edited. Content may change prior to final publication. Citation information: DOI 10.1109/TPWRS.2022.3175933, IEEE Transactions on Power Systems

microgrids 1-3 (other microgrids are isolated) obtained from the Enhanced Microgrid Power Flow (EMPF, a centralized Netwon-based microgrids power flow solver) [23] and those from our distributed APF. The voltage profiles obtained from APF are nearly identical to those from EMPF, which validates the correctness of the devised APF method.

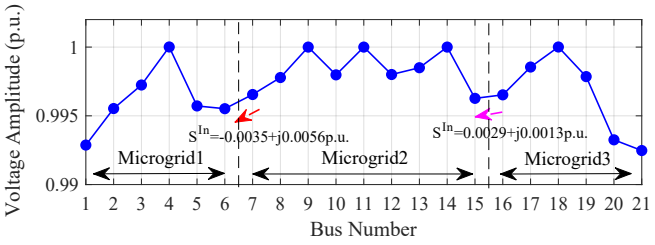

(a) Bus voltages in AC microgrids

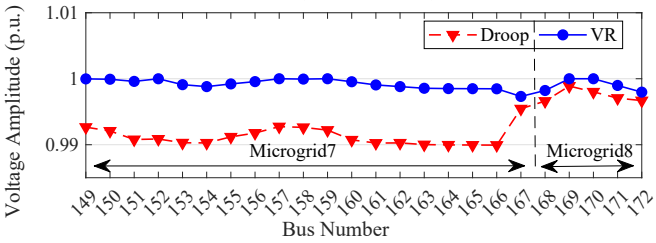

(b) Bus voltages in DC microgrids

Fig. 10: VR-APF voltage profiles

TABLE V: Microgrids 1-3 under VR mode: Voltages obtained from the centralized EMPF vs. those from the distributed APF

Bus	EMPF/APF	Bus	EMPF/APF	Bus	EMPF/APF
4	1.0000/ 1.0000	11	1.0000/ 1.0000	18	1.0000/ 1.0000
45	1.0000/ 1.0000	8	0.9938/ 0.9938	59	0.9999/ 0.9999
2	0.9955/ 0.9955	9	0.9956/ 0.9955	36	0.9999/ 0.9999
3	0.9972/ 0.9972	10	0.9957/ 0.9957	19	0.9978/ 0.9978
5	0.9949/ 0.9950	12	0.9970/ 0.9970	20	0.9932/ 0.9933
6	0.9940/ 0.9940	13	0.9973/ 0.9972	21	0.9924/ 0.9924
22	0.9944/ 0.9945	14	0.9984/ 0.9985	25	0.9984/ 0.9984
23	0.9980/ 0.9981	15	0.9953/ 0.9953	26	0.9957/ 0.9956
1	0.9928/ 0.9929	24	0.9969/ 0.9969	30	0.9999/ 0.9999
28	1.0000/ 1.0000	29	0.9955/ 0.9955	31	0.9973/ 0.9973
32	0.9986/ 0.9986	34	0.9900/ 0.9900	35	0.9958/ 0.9958
33	0.9944/ 0.9944	39	0.9887/ 0.9887	16	0.9961/ 0.9961
37	0.9981/ 0.9981	48	0.9811/ 0.9810	40	0.9947/ 0.9948
38	0.9930/ 0.9930	49	0.9820/ 0.9820	41	0.9926/ 0.9927
42	1.0000/ 1.0000	50	0.9860/ 0.9861	57	0.9946/ 0.9946
43	0.9978/ 0.9978	51	0.9855/ 0.9855	58	0.9980/ 0.9981
44	0.9982/ 0.9982	52	0.9872/ 0.9872	17	0.9984/ 0.9985
46	0.9975/ 0.9975	53	0.9860/ 0.9860	60	0.9913/ 0.9914
47	0.9911/ 0.9912	54	0.9866/ 0.9866	61	0.9901/ 0.9901
63	0.9961/ 0.9961	55	0.9828/ 0.9828	62	0.9894/ 0.9894
64	0.9872/ 0.9872	56	0.9818/ 0.9818	66	0.9946/ 0.9947
68	0.9961/ 0.9961	65	0.9832/ 0.9832	67	0.9895/ 0.9895
69	0.9872/ 0.9872	7	0.9930/ 0.9930	71	0.9947/ 0.9947
27	1.0000/ 1.0000	70	0.9832/ 0.9832	72	0.9895/ 0.9895
er	0.01%	er	0.01%	er	0.01%

4) APF Results under Different Structures: Connection schemes also influence the networked microgrids power flow. For comparison, four different system structures are studied:

- PS0$_{single}$, where 8 microgrids are interlinked by closing "single-circle" switches $[1, 2, 3, 4, 5, 6]$;
- PS0$_{double}$, where switches $[7, 8, 9, 10, 11, 12]$ are additionally closed (i.e., "double-circle" switches);
- PS1$_{single}$, where load 39 is doubled under "single-circle" switches such that the power interchanges between microgrid 1, 2 and 3 increase, as compared with PS0$_{single}$;
- PS1$_{double}$, where load 39 is doubled on top of PS0$_{double}$ with "double-circle" switches.

Simulation results are presented in Fig. 11. The comparison between "single-circle" structure and "double-circle" structure shows that a stronger connectivity in networked microgrids leads to better voltage profiles. For example, voltages in PS1$_{double}$ are smoother than those in PS1$_{single}$. The reason is that in PS1$_{double}$, tie lines S2 and S8 equally share the interface power between Microgrids 1 and 2, whereas in PS1$_{single}$ only S2 carries out the same amount of power transfer. This leads to a locally stressed Microgrid 1 in PS1$_{single}$. Similarly, the voltage profile of Microgrid 1 in PS0$_{single}$ is more variable than that in PS0$_{double}$ as shown in Fig. 11.

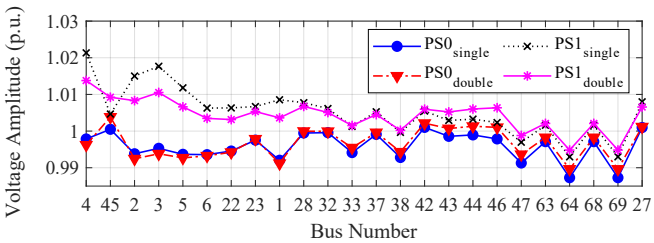

Fig. 11: PS-APF voltage profiles under single-/double-circle structures

5) APF Results under Mixed control modes: This subsection investigates the effects of mixed VR/PS modes in the eight-microgrid test system where microgrids 1-3 are interconnected and otherwise isolated. Two cases are studied in the following:

- Both PS and VR exist within a single microgrid: it is assumed that microgrid 1 is operating with both PS and VR modes. As shown in Fig. 12, the mixed VR/PS modes function properly in one microgrid without any conflict between the two. For example, the DER at bus 4 is operating under the VR mode, and its voltage is recovered to the nominal value through the coordination of tie line S2. Meanwhile, the DER at bus 45 is controlled by PS mode, and it adjusts the voltage of the local boundary bus 47 to achieve the scheduled power interchange through tie line 8.

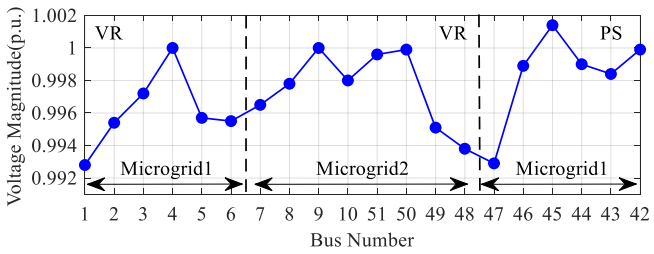

Fig. 12: Voltage profiles of microgrids 1-3: Mixed VR/PS modes within microgrids 1

- Some microgrids are under the PS mode and some under the VR mode: here, microgrid 3 is operated under the PS mode and microgrid 1 is controlled by the VR mode. Again, the

This article has been accepted for publication in a future issue of this journal, but has not been fully edited. Content may change prior to final publication. Citation information: DOI 10.1109/TPWRS.2022.3175933, IEEE Transactions on Power Systems

APF algorithm works perfectly and each control mode can achieve its control target without any conflict. For example, as shown in Fig. 13, the DER at bus 4 in the VR-based microgrid 1 can reach the nominal value by coordinating with microgrid 2. Meanwhile, the PS-based microgrid 3 could provide power support for microgrid 2 by controlling the power interchange of tie line S9.

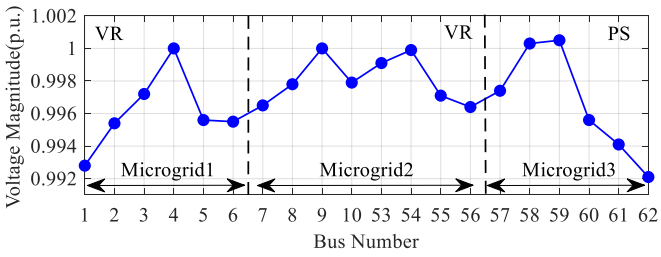

Fig. 13: Voltage profiles in microgrids 1-3: a hybrid of VR-controlled microgrids 1 and PS-controlled microgrid 3

C. Convergence Performance of APF

Table VI summarizes the convergence performance in different control modes. Fig. 14 shows the convergence performance of double-circle connected microgrids 1-3 under the VR mode.

TABLE VI: CPU time and iteration numbers

	Grid	Droop	VR	PS0	PS1
Iter	AC1-6	4	44/51 [1]	4/4	5/5
	DC7	3	33/33	3/3	3/3
	DC8	3	3/3	3/3	3/3
Time(s)	-	0.34	62.1/71.24	3.02/2.24	2.93/2.54

[1] results of "single-circle" structure / results of "double-circle" structure.

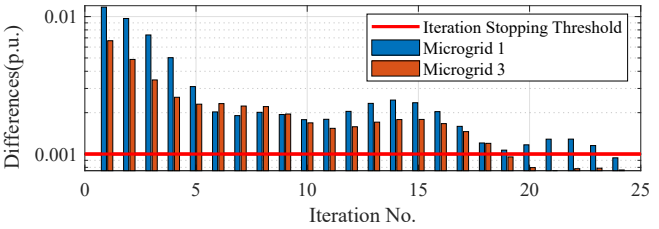

Fig. 14: Convergence of VR-APF under the double-circle structure

The following insights can be obtained:

- Networked microgrids' configurations have less impacts on the convergence of PS-based APF. For instance, it takes each single-circle connected Microgrid 5 iterations to reach convergence, same as the number of iterations for a double-circle connected microgrid to converge.
- The larger the scale of VR-based networked microgrids, the more iterations are required to reach convergence. For instance, it takes VR-based APF 51 iterations to reach convergence in the eight-microgrid system (see Table VI). Nevertheless, with Microgrids 1-3 operating in the VR mode and the rest of the system plugged out, only 24 iterations are needed to achieve the convergence (see Fig.14).
- Under the VR mode, increasing the number of tie lines raise the amount of iterations. For instance, it takes the double-circle-connected microgrids 51 more iterations to reach convergence, compared to the number of iterations needed for the single-circle-connected microgrids to converge. The reason is that more iterations are required to find an equilibrium point when more tie lines correspondingly achieve specific power interchanges.
- The convergence performance of VR-based APF can be improved by the proper setting of step sizes. Fig. 15 presents the iterations of VR-based APF under different step sizes. When the step size is set as about 100% of $\boldsymbol{S}^{Ls}/\boldsymbol{V}_{base}$, the number of iterations in the double-circle-connected microgrids 1-3 can be decreased to 13.

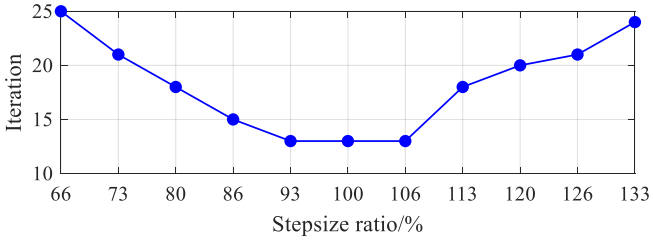

Fig. 15: Convergence performance of the double-circle structure under different step sizes

D. Operating Regions of Networked Microgrids via CPF$^+$

Fig. 16 shows three typical operating region nomograms for Microgrid 2 provided by our CPF$^+$ tool. The idea is to select a number of system stability features and translate voltage stability to those features such as multiple P/f droop coefficients, multiple Q/V droop coefficients, and power delivery from Microgrid 2 to Microgrids 1 and 3. Such information offers valuable early warning and safety indicators for microgrid operators. The following insights can be obtained:

- Extreme power transfer can significantly reduce the operating limit of DER droop coefficients for maintaining static voltage stability. As shown in Fig. 16(a), when Microgrid 2 transfers 0.0862 p.u. of active power to Microgrid 1 as well as 0.0862 p.u. to Microgrid 3, the margin of the P/f droop coefficient decreases to 1.3.
- Fig. 16(b) indicates that the droop margin is relatively insensitive to the locations where power interchanges occur. Rather, it is the total amount of power interchanges that matter most. For instance, as long as the total power interchange is 0.0862 p.u., no matter Microgrid 2's power is transferred to Microgrid 1, Microgrid 3, or both, the Q/V droop margin remains around 21.7.
- Fig. 16(c) illustrates a remarkable positive correlation between the operating limit of power interchange and both P/f and Q/V droop coefficients. For instance, when P/f and Q/V droop coefficients are both set as 0.33 p.u., the limit of power interchange margin factor is 25.3 higher than that with both coefficients set as 0.12 p.u..

E. Verifying Networked Microgrids Reconfiguration

Reconfiguration alters networked microgrids for improving system performances, e.g., voltage profiles and voltage stability. The purpose of this subsection is to verify the potential usefulness of APF and CPF$^+$ in reconfiguration applications.

This article has been accepted for publication in a future issue of this journal, but has not been fully edited. Content may change prior to final publication. Citation information: DOI 10.1109/TPWRS.2022.3175933, IEEE Transactions on Power Systems

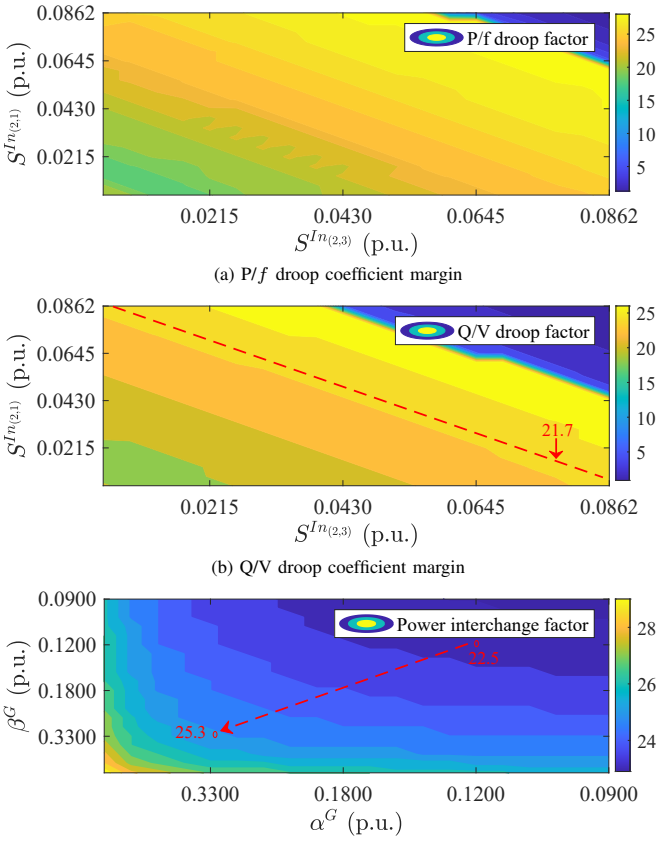

(a) P/f droop coefficient margin

(b) Q/V droop coefficient margin

(c) Power interchange margin

Fig. 16: Feasible operating region of Microgrid 2 via CPF$^+$.

An example of the reconfiguration objective is to minimize power losses and voltage variations by changing the on/off status of tie switches:

$$Obj = \min \sum_{j=1}^{N_{MG}} [\|S_j^{Gs} - S_j^{Ls} - S_j^{Ins}\| + \sum_{i=1}^{N_j} \|V^* - V_i\|] \quad (23)$$

Correspondingly, the optimal, an average and the worst configurations are identified with objectives being 7.9248, 12.2077 and 16.2243, respectively. The switches (1-12) status are $[1,1,1,1,1,1,1,1,1,0,1,0]$, $[0,1,0,1,1,1,1,1,1,1,0,1,1]$, $[0,1,0,1,1,0,0,1,1,0,1,0]$, accordingly.

Fig. 17 provides the voltage profiles (i.e., taking Microgrids 3 and 6 as examples) under different system configurations. It can be observed that the optimally configured networked microgrids have improved voltage profiles. For instance, the voltages in Microgrids 3 and 6 are maintained consistently close to the nominal value. Reconfiguration also impacts the power interchange margin. The power interchange margin with optimized configuration is higher than that in the worst scenario. This is because the voltage profile in the worst configuration is inferior to that in optimal configuration, which compromises DER buses' capabilities to adjust voltages and transfer power to neighboring microgrids.

F. Scalability Validation of APF

In the following subsection, the scalability of APF is further verified on a large networked microgrids test system. As illustrated in Fig. 18, the three-microgrid test system is established by modifying the IEEE 906-bus low voltage distribution

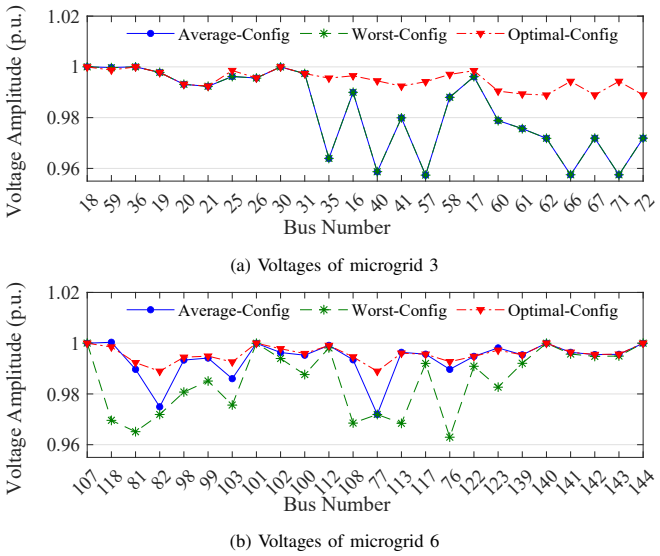

(a) Voltages of microgrid 3

(b) Voltages of microgrid 6

Fig. 17: Voltage profiles under different networked microgrid configurations

system. Table VII presents the droop coefficients of DERs in the test system. Detailed parameters of lines and loads can be found in [43].

TABLE VII: Droop coefficients of DERs in the 906-bus system (p.u.)

Bus	195	100	282	550	453	330	428	712	838
m/n	0.2	0.3	0.6	0.1	1	1	0.2	1	1

- Fig. 19 illustrates the effectiveness of the VR-APF in large systems. For example, the voltage of DER bus 195 can be recovered to the nominal value through power coordination between the microgrids 1 and 2.

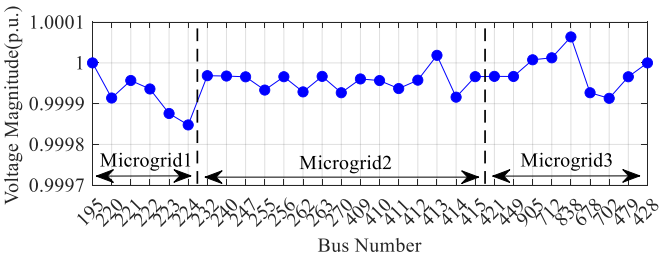

Fig. 19: Voltage profiles of VR-based microgrids

- The efficacy of PS-based APF is validated in the large system. For example, Fig. 20 presents the microgrid voltage profiles of the test system under the PS mode. When microgrid 2 suffers the power deficiency, the voltage of boundary bus 421 in microgrid 3 is enhanced to drive the power injections into microgrid 2.

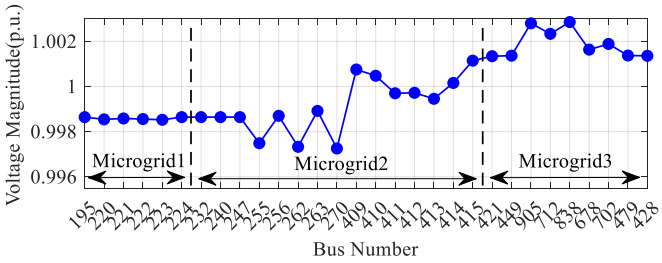

Fig. 20: Voltage profiles of PS-controlled microgrids

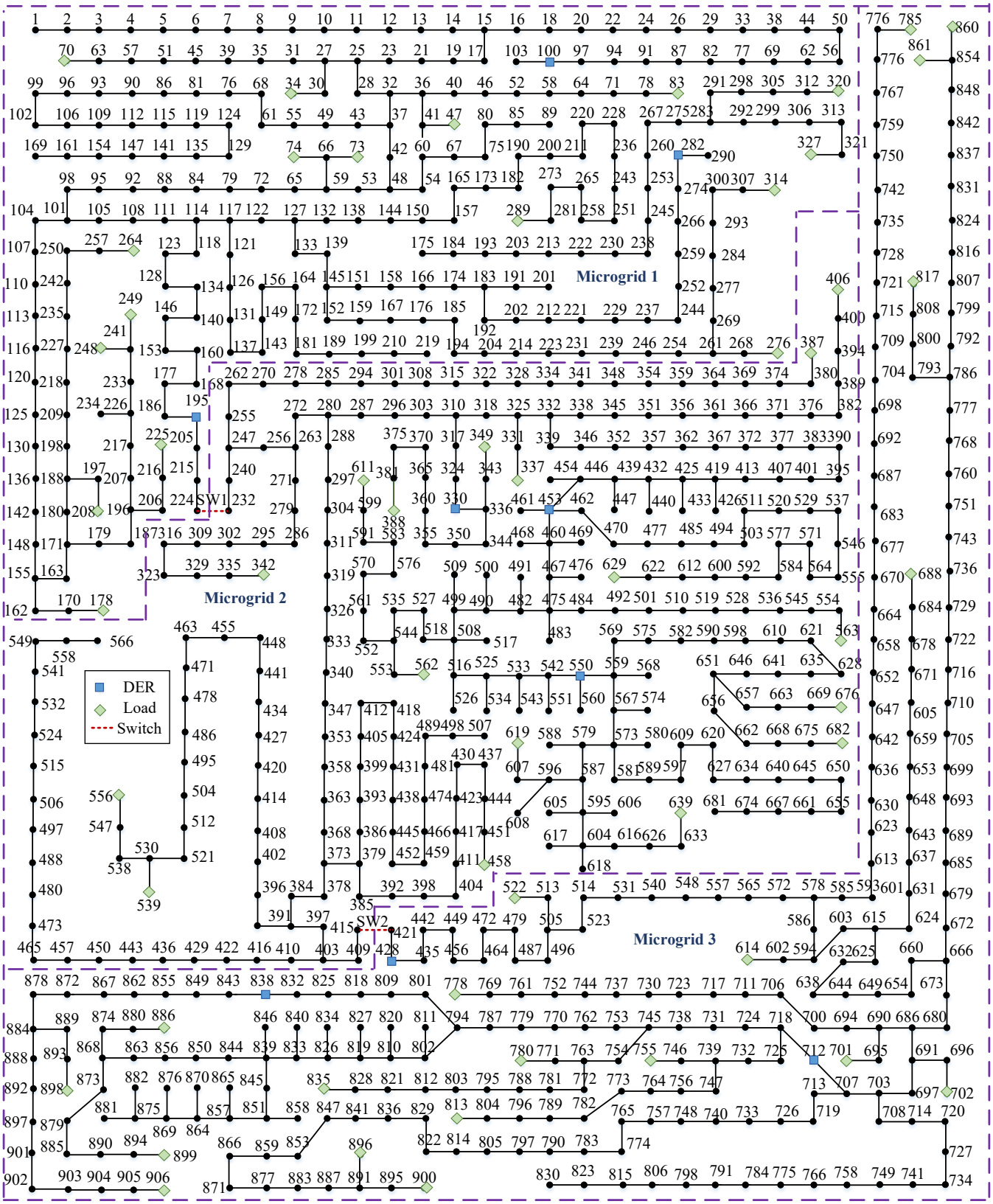

Fig. 18: A 906-bus, three-microgrid test system modified from the IEEE European low-voltage distribution system. Base voltage: 416 V. Base power: 19 KVA

- Meanwhile, the performance of the mixed PS/VR modes is investigated in Fig. 21. It verifies the capability of the APF method in solving large networked microgrids equipped with different control modes. For example, the voltage of DER bus 428 in microgrid 3 correctly achieves the nominal value. Meanwhile, the voltage difference across the tie line shows obviously that PS-based microgrid 1 can receive power support from microgrid 2 by adjusting the power interchange through switch 1.

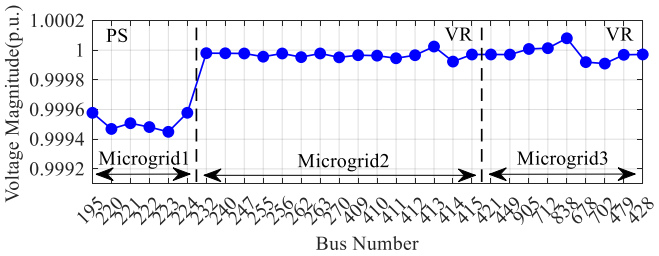

Fig. 21: Voltage profiles of hybrid VR/PS-controlled microgrids

- The scalability of APF is also validated by examining its convergence performances on test systems at different scales. For instances, APF converges with 51 iterations for solving the 342-bus networked microgrids system and 76 iterations for the 906-bus network.

V. Conclusion

APF has been developed for accurately integrating hierarchical control modes in networked microgrids power flow. CPF$^+$ further allows for voltage stability assessment of networked microgrids through power flow calculation. Case studies demonstrate the capability of APF in handling arbitrary network structures and multiconnected microgrid clusters. The distributed solution scheme for APF and CPF$^+$ renders privacy protection solutions for community microgrids to coordinate and manage microgrids and DERs safely and securely. Thus, both tools are promising to be implemented in energy management systems of networked community microgrids.

VI. Appendix

In the Appendix, detailed line parameters and loads of the eight-microgrid test system in Subsection IV.B are provided in Tables VIII and IX, respectively.

TABLE VIII: Line parameters of the eight-microgrid test system

From	To	R	X	From	To	R	X
1	2	0.000651	0.000915	16	17	0.000651	0.000915
2	3	0.000163	0.000229	17	18	0.000163	0.000229
3	4	0.000163	0.000229	18	19	0.000163	0.000229
4	5	0.000651	0.000915	19	20	0.000651	0.000915
5	6	0.000651	0.000915	20	21	0.000651	0.000915
42	43	0.000651	0.000915	57	58	0.000651	0.000915
43	44	0.000163	0.000229	58	59	0.000163	0.000229
44	45	0.000651	0.000915	59	60	0.000651	0.000915
45	46	0.000163	0.000229	60	61	0.000163	0.000229
46	47	0.000651	0.000915	61	62	0.000651	0.000915
1	22	0.000651	0.000915	16	25	0.000651	0.000915
22	27	0.000651	0.000915	25	30	0.000163	0.000229
27	32	0.000163	0.000229	30	35	0.000651	0.000915
32	37	0.000163	0.000229	35	40	0.000163	0.000229
37	42	0.000651	0.000915	40	57	0.000651	0.000915
42	63	0.000651	0.000915	57	66	0.000651	0.000915
63	68	0.000651	0.000915	66	71	0.000163	0.000229
6	23	0.000651	0.000915	21	26	0.000651	0.000915
23	28	0.000163	0.000229	26	31	0.000163	0.000229
28	33	0.000651	0.000915	31	36	0.000163	0.000229
33	38	0.000163	0.000229	36	41	0.000651	0.000915
38	47	0.000651	0.000915	41	62	0.000651	0.000915
47	64	0.000651	0.000915	62	67	0.000651	0.000915
64	69	0.000163	0.000229	67	72	0.000163	0.000229
83	84	0.000651	0.000915	98	99	0.000651	0.000915
84	85	0.000163	0.000229	99	100	0.000163	0.000229
85	86	0.000651	0.000915	100	101	0.000651	0.000915
86	87	0.000163	0.000229	101	102	0.000163	0.000229
87	88	0.000651	0.000915	102	103	0.000651	0.000915
124	125	0.000651	0.000915	139	140	0.000651	0.000915
125	126	0.000163	0.000229	140	141	0.000651	0.000915
126	127	0.000651	0.000915	141	142	0.000163	0.000229
127	128	0.000163	0.000229	142	143	0.000163	0.000229
128	129	0.000651	0.000915	143	144	0.000651	0.000915
73	78	0.000163	0.000229	76	81	0.000163	0.000229
78	83	0.000651	0.000915	81	98	0.000651	0.000915
83	104	0.000651	0.000915	98	107	0.000651	0.000915
104	109	0.000651	0.000915	107	112	0.000163	0.000229
109	114	0.000163	0.000229	112	117	0.000651	0.000915
114	119	0.000163	0.000229	117	122	0.000163	0.000229
119	124	0.000651	0.000915	122	139	0.000651	0.000915
74	79	0.000163	0.000229	77	82	0.000651	0.000915
79	88	0.000651	0.000915	82	103	0.000651	0.000915
88	105	0.000651	0.000915	103	108	0.000651	0.000915
105	110	0.000163	0.000229	108	113	0.000163	0.000229
110	115	0.000651	0.000915	113	118	0.000163	0.000229
115	120	0.000163	0.000229	118	123	0.000651	0.000915
7	8	0.000163	0.000229	75	80	0.000163	0.000229
8	9	0.000163	0.000229	80	93	0.000651	0.000915
9	10	0.000651	0.000915	93	106	0.000651	0.000915
10	11	0.000651	0.000915	106	111	0.000163	0.000229
11	12	0.000651	0.000915	111	116	0.000651	0.000915
12	13	0.000163	0.000229	116	121	0.000163	0.000229
13	14	0.000163	0.000229	121	134	0.000651	0.000915
14	15	0.000651	0.000915	89	90	0.000163	0.000229
48	49	0.000163	0.000229	90	91	0.000651	0.000915
49	50	0.000651	0.000915	91	92	0.000163	0.000229
50	51	0.000163	0.000229	92	93	0.000651	0.000915
51	52	0.000651	0.000915	93	94	0.000651	0.000915
52	53	0.000651	0.000915	94	95	0.000163	0.000229
53	54	0.000163	0.000229	95	96	0.000651	0.000915
54	55	0.000651	0.000915	96	97	0.000163	0.000229
55	56	0.000163	0.000229	130	131	0.000651	0.000915
11	24	0.000651	0.000915	131	132	0.000163	0.000229
24	29	0.000163	0.000229	132	133	0.000163	0.000229
29	34	0.000651	0.000915	133	134	0.000651	0.000915
34	39	0.000163	0.000229	134	135	0.000651	0.000915
39	52	0.000651	0.000915	135	136	0.000651	0.000915
52	65	0.000651	0.000915	136	137	0.000163	0.000229
65	70	0.000163	0.000229	137	138	0.000163	0.000229

References

[1] P. Zhang, B. Wang, P. B. Luh, L. Ren, and Y. Qin, "Enabling resilient microgrid through ultra-fast programmable network," US Patent US10505853, 2019. [Online]. Available: https://patents.google.com/patent/US10505853B2/en

[2] J. Li, Y. Liu, and L. Wu, "Optimal operation for community-based multi-party microgrid in grid-connected and islanded modes," *IEEE Transactions on Smart Grid*, vol. 9, no. 2, pp. 756–765, 2018.

[3] M. A. Allam, A. A. Hamad, and M. Kazerani, "A generic modeling and power-flow analysis approach for isochronous and droop-controlled microgrids," *IEEE Transactions on Power Systems*, vol. 33, no. 5, pp. 5657–5670, 2018.

[4] L. Ren, Y. Qin, Y. Li, P. Zhang, B. Wang, P. B. Luh, S. Han, T. Orekan, and T. Gong, "Enabling resilient distributed power sharing in networked microgrids through software defined networking," *Applied Energy*, vol. 210, pp. 1251–1265, 2018. [Online]. Available: https://www.sciencedirect.com/science/article/pii/S0306261917307560

TABLE IX: Loads in the eight-microgrid system

Bus	2	3	5	6	22	23	1	32
P/kW	47.18	47.61	46.33	45.46	45.19	44.98	48.91	44.97
Q/kVar	32.09	32.38	30.98	31.13	28.70	27.63	32.26	27.13
Bus	37	38	42	43	46	47	63	64
P/kW	44.03	44.38	45.48	45.91	45.88	46.28	44.61	44.86
Q/kVar	28.00	28.27	29.89	29.80	29.98	30.60	29.39	30.25
Bus	11	8	10	12	13	15	24	39
P/kW	46.36	45.4	46.55	46.51	48.29	47.02	43.83	44.51
Q/kVar	29.39	29.28	30.05	29.19	29.09	29.04	27.10	28.92
Bus	48	51	52	53	56	65	7	18
P/kW	45.44	44.41	45.53	45.11	45.29	45.03	45.40	47.24
Q/kVar	29.66	27.75	27.14	26.53	27.23	29.64	28.97	27.74
Bus	19	20	21	25	26	31	16	40
P/kW	47.71	45.31	46.48	43.86	44.17	43.41	45.90	44.96
Q/kVar	28.79	27.17	28.65	25.49	26.46	26.12	27.29	30.05
Bus	41	57	58	17	60	61	62	66
P/kW	45.95	44.31	46.91	46.07	44.02	47.86	44.91	42.71
Q/kVar	30.26	26.78	29.50	27.04	26.80	30.44	29.83	26.17
Bus	67	78	79	83	84	87	88	104
P/kW	43.11	45.47	45.19	45.03	44.60	45.76	45.80	44.56
Q/kVar	27.06	26.21	25.96	24.42	25.90	26.76	28.11	25.09
Bus	105	73	114	120	124	125	127	128
P/kW	44.36	45.33	46.12	45.83	45.15	46.19	47.05	46.81
Q/kVar	26.07	28.38	27.24	27.65	29.85	30.11	28.04	26.99
Bus	129	132	137	80	89	92	93	94
P/kW	46.34	45.53	46.70	45.82	45.77	47.45	47.58	47.31
Q/kVar	25.17	26.68	31.20	26.14	27.80	28.48	27.92	26.44
Bus	97	106	121	130	133	134	138	135
P/kW	47.01	46.81	44.94	47.09	45.26	45.25	46.1	45.67
Q/kVar	25.28	28.33	28.16	26.75	26.62	28.64	29.49	29.55
Bus	107	81	82	98	99	103	102	108
P/kW	45.85	45.23	45.00	46.27	46.15	44.43	45.29	46.60
Q/kVar	27.68	24.81	24.89	23.46	23.67	23.66	23.87	27.70
Bus	113	122	123	139	140	142	143	144
P/kW	46.57	46.15	44.28	47.58	47.57	46.74	44.91	43.36
Q/kVar	27.69	30.77	29.41	28.75	29.70	29.37	28.40	27.47

[5] Z. Tang, P. Zhang, W. O. Krawec, and Z. Jiang, "Programmable quantum networked microgrids," *IEEE Transactions on Quantum Engineering*, vol. 1, pp. 1–13, 2020.

[6] Y. Zhou, P. Zhang, and M. Yue, "Reachable dynamics of networked microgrids with large disturbances," *IEEE Transactions on Power Systems*, vol. 36, no. 3, pp. 2416–2427, 2021.

[7] W. Wan, M. A. Bragin, B. Yan, Y. Qin, J. Philhower, P. Zhang, and P. B. Luh, "Distributed and asynchronous active fault management for networked microgrids," *IEEE Transactions on Power Systems*, vol. 35, no. 5, pp. 3857–3868, 2020.

[8] P. Babahajiani, L. Wang, J. Liu, and P. Zhang, "Push-sum-enabled resilient microgrid control," *IEEE Transactions on Smart Grid*, vol. 12, no. 4, pp. 3661–3664, 2021.

[9] G. Davis, "Microgrid energy management system," *CERTS Program Report, Lawrence Berkeley National Laboratory, Berkeley, USA*, 2003.

[10] A. Elrayyah, Y. Sozer, and M. E. Elbuluk, "A novel load-flow analysis for stable and optimized microgrid operation," *IEEE Transactions on Power Delivery*, vol. 29, no. 4, pp. 1709–1717, Aug 2014.

[11] J. Lee, Y. Kim, and S. Moon, "Novel supervisory control method for islanded droop-based ac/dc microgrids," *IEEE Transactions on Power Systems*, vol. 34, no. 3, pp. 2140–2151, 2019.

[12] J. M. Guerrero, M. Chandorkar, T.-L. Lee, and P. C. Loh, "Advanced control architectures for intelligent microgrids—part i: Decentralized and hierarchical control," *IEEE Transactions on Industrial Electronics*, vol. 60, no. 4, pp. 1254–1262, 2013.

[13] D. Y. Yamashita, I. Vechiu, and J.-P. Gaubert, "A review of hierarchical control for building microgrids," *Renewable and Sustainable Energy Reviews*, vol. 118, p. 109523, 2020.

[14] J. W. Simpson-Porco, Q. Shafiee, F. Dörfler, J. C. Vasquez, J. M. Guerrero, and F. Bullo, "Secondary frequency and voltage control of islanded microgrids via distributed averaging," *IEEE Transactions on Industrial Electronics*, vol. 62, no. 11, pp. 7025–7038, Nov 2015.

[15] F. Mumtaz, M. H. Syed, M. A. Hosani, and H. H. Zeineldin, "A novel approach to solve power flow for islanded microgrids using modified newton raphson with droop control of DG," *IEEE Transactions on Sustainable Energy*, vol. 7, no. 2, pp. 493–503, April 2016.

[16] G. C. Kryonidis, E. O. Kontis, A. I. Chrysochos, K. O. Oureilidis, C. S. Demoulias, and G. K. Papagiannis, "Power flow of islanded ac microgrids: Revisited," *IEEE Transactions on Smart Grid*, vol. 9, no. 4, pp. 3903–3905, 2018.

[17] M. A. Allam, A. A. Hamad, and M. Kazerani, "A sequence-component-based power-flow analysis for unbalanced droop-controlled hybrid ac/dc microgrids," *IEEE Transactions on Sustainable Energy*, vol. 10, no. 3, pp. 1248–1261, July 2019.

[18] A. Garcés, "On the convergence of Newton's method in power flow studies for dc microgrids," *IEEE Transactions on Power Systems*, vol. 33, no. 5, pp. 5770–5777, Sep. 2018.

[19] A. A. Hamad, M. A. Azzouz, and E. F. El Saadany, "A sequential power flow algorithm for islanded hybrid ac/dc microgrids," *IEEE Transactions on Power Systems*, vol. 31, no. 5, pp. 3961–3970, Sep. 2016.

[20] A. Gupta, S. Doolla, and K. Chatterjee, "Hybrid ac–dc microgrid: Systematic evaluation of control strategies," *IEEE Transactions on Smart Grid*, vol. 9, no. 4, pp. 3830–3843, 2018.

[21] A. A. Eajal, M. A. Abdelwahed, E. F. El-Saadany, and K. Ponnambalam, "A unified approach to the power flow analysis of ac/dc hybrid microgrids," *IEEE Transactions on Sustainable Energy*, vol. 7, no. 3, pp. 1145–1158, July 2016.

[22] E. Aprilia, K. Meng, M. Al Hosani, H. H. Zeineldin, and Z. Y. Dong, "Unified power flow algorithm for standalone ac/dc hybrid microgrids," *IEEE Transactions on Smart Grid*, vol. 10, no. 1, pp. 639–649, Jan 2019.

[23] F. Feng and P. Zhang, "Enhanced microgrid power flow incorporating hierarchical control," *IEEE Transactions on Power Systems*, vol. 35, no. 3, pp. 2463–2466, 2020.

[24] G. Díaz, J. Gómez-Aleixandre, and J. Coto, "Direct backward/forward sweep algorithm for solving load power flows in ac droop-regulated microgrids," *IEEE Transactions on Smart Grid*, vol. 7, no. 5, pp. 2208–2217, Sep. 2016.

[25] L. Ren and P. Zhang, "Generalized microgrid power flow," *IEEE Transactions on Smart Grid*, vol. 9, no. 4, pp. 3911–3913, July 2018.

[26] F. Feng and P. Zhang, "Implicit Z_{bus} Gauss algorithm revisited," *IEEE Transactions on Power Systems*, vol. 35, no. 5, pp. 4108–4111, 2020.

[27] Y. Zhou and P. Zhang, "Reachable power flow," *IEEE Transactions on Power Systems*, vol. 35, no. 4, pp. 3290–3293, 2020.

[28] ——, "Reachable power flow: Theory to practice," *IEEE Transactions on Power Systems*, vol. 36, no. 3, pp. 2532–2541, 2021.

[29] P. Zhang, *Networked Microgrids*. Cambridge, UK: Cambridge University Press, 2021.

[30] P. S. Nirbhavane, L. Corson, S. M. H. Rizvi, and A. K. Srivastava, "TPCPF: Three-phase continuation power flow tool for voltage stability assessment of distribution networks with distributed energy resources," *IEEE Transactions on Industry Applications*, vol. 57, no. 5, pp. 5425–5436, 2021.

[31] H. Sheng and H.-D. Chiang, "CDFLOW: A practical tool for tracing stationary behaviors of general distribution networks," *IEEE Transactions on Power Systems*, vol. 29, no. 3, pp. 1365–1371, 2014.

[32] X. Dou, S. Zhang, L. Chang, Z. Wu, W. Gu, M. Hu, and X. Yuan, "An improved CPF for static stability analysis of distribution systems with high DG penetration," *International Journal of Electrical Power, Energy Systems*, vol. 86, pp. 177–188, 2017.

[33] Y. Ju, W. Wu, and B. Zhang, "Loop-analysis-based continuation power flow algorithm for distribution networks," *Generation, Transmission, Distribution, IET*, vol. 8, pp. 1284–1292, 07 2014.

[34] M. Abdel-Akher, "Voltage stability analysis of unbalanced distribution systems using backward/forward sweep load-flow analysis method with secant predictor," *Generation, Transmission, Distribution, IET*, vol. 7, pp. 309–317(8), 03 2013.

[35] H.-T. Kim, J. Lee, M. Yoon, M.-J. Lee, N. Cho, and S. Choi, "Continuation power flow based distributed energy resource hosting capacity estimation considering renewable energy uncertainty and stability in distribution systems," *Energies*, vol. 13, no. 17, 2020.

[36] V. Ajjarapu and C. Christy, "The continuation power flow: a tool for steady state voltage stability analysis," *IEEE Transactions on Power Systems*, vol. 7, no. 1, pp. 416–423, 1992.

[37] X.-P. Zhang, P. Ju, and E. Handschin, "Continuation three-phase power flow: a tool for voltage stability analysis of unbalanced three-phase power systems," *IEEE Transactions on Power Systems*, vol. 20, no. 3, pp. 1320–1329, 2005.

[38] Z. Pan, H. Fu, P. Hou, and X. Tong, "Continuous power flow of islanded microgrids with droop-controlled distributed generations," in *2019 IEEE International Conference on Enerfengy Internet (ICEI)*, 2019, pp. 567–572.

[39] L. Wang, Y. Qin, Z. Tang, and P. Zhang, "Software-defined microgrid control: The genesis of decoupled cyber-physical microgrids," *IEEE Open Access Journal of Power and Energy*, vol. 7, pp. 173–182, 2020.
[40] J.-H. Teng, "Modelling distributed generations in three-phase distribution load flow," *IET Generation, Transmission Distribution*, vol. 2, no. 3, pp. 330–340, 2008.
[41] H. E. Farag, E. El-Saadany, R. El Shatshat, and A. Zidan, "A generalized power flow analysis for distribution systems with high penetration of distributed generation," *Electric Power Systems Research*, vol. 81, no. 7, pp. 1499 – 1506, 2011.
[42] K. Schneider, P. Phanivong, and J.-S. Lacroix, "Ieee 342-node low voltage networked test system," in *2014 IEEE PES General Meeting — Conference Exposition*, 2014, pp. 1–5.
[43] IEEE PES Distribution test feeders, "The ieee european low voltage test feeder," Patent, 03, 2020. [Online]. Available: https://site.ieee.org/pestestfeeders/resources/

Fei Feng (Graduate Student Member, IEEE) received the B.S. degree in electrical engineering from Southwest Jiaotong University, Chengdu, China, in 2016, and the M.S. degree in electrical engineering from Chongqing University, Chongqing, China, in 2019. He is currently working towards the Ph.D. degree in electrical engineering with the department of Electrical and Computer Engineering, Stony Brook University, Stony Brook, NY, USA. His research interests include networked microgrids, power flow, state estimation and quantum computing.

Peng Zhang (Senior Member, IEEE) received the Ph.D. degree in electrical engineering from the University of British Columbia, Vancouver, BC, Canada, in 2009. He is a Full Professor of Electrical and Computer Engineering, and a SUNY Empire Innovation Professor at Stony Brook University, New York. He has a joint appointment at Brookhaven National Laboratory as a Staff Scientist. Previously, he was a Centennial Associate Professor and a Francis L. Castleman Associate Professor at the University of Connecticut, Storrs, CT, USA. He was a System Planning Engineer at BC Hydro and Power Authority, Canada, during 2006-2010. His research interests include AI-enabled smart grids, quantum-engineered power grids, networked microgrids, power system stability and control, cybersecurity, and formal methods and reachability analysis. Dr. Zhang is an individual member of CIGRÉ. He is an Editor for the IEEE Transactions on Power Systems, the IEEE Power and Energy Society Letters, and the IEEE Journal of Oceanic Engineering.

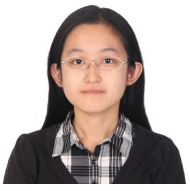

Yifan Zhou (Member, IEEE) received the B.S. degree in electrical engineering from Tsinghua University, Beijing, China, in 2014, and the Ph.D. degree in electrical engineering from Tsinghua University, Beijing, China, in 2019. She is currently a Postdoctoral Researcher with Stony Brook University, Stony Brook, NY, USA. Her research interests include microgrid stability and control, formal methods and reachability analysis, and quantum computing.

Lizhi Wang (Graduate Student Member, IEEE) received the B.S. and M.S. degrees in electrical engineering from Zhejiang University, Hangzhou, China, in 2015 and 2018, respectively. He is currently pursuing the Ph.D. degree in electrical engineering at Stony Brook University, Stony Brook, NY, USA. His current research interests include stability analysis, learning-based control for microgrids, and cyber-physical security for electric power networks.